Available online at www.sciencedirect.com

ScienceDirect

Geochimica et Cosmochimica Acta 238 (2018) 102–122

Geochimica et Cosmochimica Acta

www.elsevier.com/locate/gca

Fraction-specific rare earth elements enable the reconstruction of primary seawater signatures from iron formations

P.B.H. Oonk [a,b], P.R.D. Mason [a,*], H. Tsikos [b], M. Bau [c]

[a] Department of Earth Sciences, Utrecht University, Princetonlaan 8A, 3584CB Utrecht, The Netherlands
[b] Geology Department, Rhodes University, Artillery Road, Grahamstown 6140, South Africa
[c] Department of Physics and Earth Sciences, Jacobs University Bremen, 28759 Bremen, Germany

Received 13 December 2017; accepted in revised form 4 July 2018; available online 12 July 2018

Abstract

Rare earth element (REE) abundances in iron formations (IFs) provide key evidence to track the redox evolution of the Precambrian oceans. Deriving information about processes and sources from IFs is complicated by the variable roles of diagenetic dissolution and precipitation that modify primary depositional signals in the rocks. Iron formations are typically mineralogically heterogeneous with varying amounts of carbonate (ankerite + siderite), oxide (predominantly magnetite) and silicate (chert and Fe-silicates). To date, little is known about the respective contributions of these fractions to the bulk-rock REE signal, and which fraction most accurately records primary seawater signals. Here we evaluate an optimized sequential extraction scheme for REE analysis in the ca. 2.46 Ga Asbestos Hills IFs from the Griqualand-West Basin in South Africa. These rocks were deposited immediately before the Great Oxidation Event and are potentially an important archive for large-scale redox changes in the (near) surface environment.

To fully evaluate our method, we measured lanthanide elements plus ytrrium (REY) in individual minerals, in bulk rock samples and in three separate fractions using acetate, oxalate and total digestion sequential extractions. The extraction techniques were then verified using a mass balance approach, the first time that this has been comprehensively applied to IFs. Similarities between the carbonate fraction data and modern seawater, coupled with strong measurement reproducibility and systematic stratigraphic variability suggests that carbonate most closely tracks the primary seawater composition. The Asbestos Hills IFs show distinctive REY signatures with strongly variable $(Yb/Pr)_{SN}$ ratios, positive La anomalies, positive and constant Y/Ho, weakly positive Eu anomalies and a lack of Ce anomalies in their carbonate fraction. Stratigraphic variations in these parameters suggest deposition in a stratified fully anoxic ocean, which became shallower over time. The silicate fraction was influenced by various amounts of allochthonous material (detrital and volcanic ash), although some minerals including greenalite, minnesotaite and stilpnomelane may have tracked seawater REE variability. The oxide fraction was found to be the most REY-depleted and therefore susceptible to allochthonous influences as well as diagenetic controls. It shows a systematic MREE enrichment that has not been described in IFs before, but has been seen in sub-oxic, ferrous environments. An increase in the ratio of carbonate to oxide minerals ongoing upwards through the Asbestos Hills IF, from deep to shallow water conditions, most likely reflected an increase in dissimilatory iron reduction close to the margin of the anoxic basin.

Keywords: Iron formation; Transvaal supergroup; Sequential extraction; Rare earth elements; Great oxidation event

* Corresponding author.
E-mail address: p.mason@uu.nl (P.R.D. Mason).

https://doi.org/10.1016/j.gca.2018.07.005
0016-7037/

1. INTRODUCTION

Iron formations (IFs) were deposited as marine chemical precipitates throughout the Archean and Paleoproterozoic, and have the potential to help reconstruct deep-time secular changes in seawater chemistry (e.g. Bekker et al., 2010; Konhauser et al., 2017). Accurate determination of surface environmental conditions based on IF chemistry is challenging since primary seawater signals can be difficult to resolve due to the input of allochtonous material and the potential for open system exchange during post-depositional processes, such as during diagenetic dissimilatory iron reduction or alteration. In general, IF samples are mineralogically heterogeneous as a result of various processes including primary precipitation (e.g. Beukes, 1984; Rasmussen et al., 2015), detrital input (e.g. Bau, 1993), diagenetic reworking (Johnson et al., 2008; Heimann et al., 2010) and/or re-equilibration with pore waters (Alibert, 2016).

The IFs deposited around the Great Oxidation Event (GOE; e.g. Canfield, 2005) at 2.4 to 2.3 Ga provide critical data for tracing the evolution of seawater chemistry during atmospheric oxygenation. The Asbestos Hills IFs of the Transvaal Supergroup in South Africa were deposited immediately before the GOE around 2.52–2.43 Ga (Trendall et al., 1990; Sumner and Bowring, 1996; Pickard, 2003; Gumsley et al., 2017) and are a key archive of chemical data for marine systems prior to, or at the beginning of global oxygenation. The low metamorphic grade of the IFs (<150 °C, Miyano and Beukes, 1984), combined with the pristine nature of geochemical signals in underlying carbonate rocks of the Campbellrand Subgroup (Eroglu et al., 2017), makes these rocks a prime target to unravel how depositional and (post)diagenetic processes might affect the mineralogy and chemistry of IFs.

One of the key geochemical tools currently used to argue for direct chemical precipitation of IF minerals from seawater comes from shale-normalized rare earth elements (REE-typically refers to the lanthanide elements only) and REE + yttrium (REY) patterns. Rare earth elements in present-day seawater are controlled by differences in terrestrial versus hydrothermal input and by particle-solution interactions (e.g. Elderfield et al., 1988; Byrne and Kim, 1990; Derry and Jacobsen, 1990; Bolhar et al., 2004). Particle reactivity is a function of water depth, salinity and the local redox state. Although no direct measurements of ancient seawater are possible, similarities between unmetamorphosed bulk rock IF data and modern seawater (e.g. Derry and Jacobsen, 1990; Bau, 1993; Bau and Dulski, 1996; Bolhar et al., 2004; Frei et al., 2008; Planavsky et al., 2010; Delvigne et al., 2012) suggests that a primary REY signature can be captured into bulk IF and indicates that post-depositional REY modification is minor (Bau and Dulski, 1996). Similar mineralogical and biological controls could have therefore controlled REE distribution in the ferruginous Paleoproterozoic ocean as in modern oxic seawater, although this hypothesis requires further testing.

Iron formation samples contain three different rare earth element-hosting fractions: the Fe-carbonates, Fe-oxides and Fe-silicates that each potentially fractionate REY in different ways. The bulk rock REY data currently used for investigating seawater processes is therefore controlled by the relative abundance of these three fractions. Furthermore, chemostratigraphic comparisons are not easily done between rocks with contrasting mineralogy. Therefore, mineral-specific REE data can potentially help identify specific processes during mineral formation during both primary precipitation and post-depositional modification. Physical separation of individual minerals in IF is practically unattainable due to the very-fine grained textural nature. Focussing on mono-mineralogical samples obtained by micro-drilling could be a valid approach (e.g. Bau and Alexander, 2009; Viehmann et al., 2015), but most bands in IFs do not consist of a single mineral fraction. Work done on an even smaller scale can be influenced by micro- or nano- inclusions in large crystals (e.g. Li et al., 2011).

In recent years, REY data have been produced for individual minerals from IF using in-situ microanalytical techniques, such as Laser Ablation ICP-MS. Apatite REE were used to constrain the origin of the Eoarchean Isua IFs (Lepland et al., 2002). LA-ICP-MS analysis of various minerals (incl. magnetite) in the metamorphosed IFs of the Nuvvuagittuq Supracrustal Belt helped to constrain IF paragenesis and its suitability as a 3.8 Ga seawater proxy (Mloszewska et al., 2012). In a recent paper, IF magnetite REY data from the 3.1–3.3 Ga Badampahar Greenstone belt was used to model paleo-seawater concentrations (Ghosh and Baidya, 2017). Alibert (2016) produced mineral-specific REE patterns in the Dales Gorge IFs representative for typical, unmetamorphosed IFs, in an attempt to constrain pathways for mineral formation. The latter study concluded that many minerals do not show seawater-like REE patterns, but display features better explained by equilibration with pore-waters during early diagenesis (Alibert, 2016). Although these studies have made new insights, the focus on microanalytical data alone can be problematic since small-scale heterogeneities can obscure the identification of larger scale trends. In addition, analysis is often limited to larger mineral grains that may bias results towards restricted generations of crystallization and specific processes.

Here we attempt to resolve some of these issues by applying a sequential extraction scheme for REY analysis in bulk powdered IF (Poulton and Canfield, 2005). Similar sequential extraction methods have been successfully applied to better understand REE fractionation between seawater and hydrogenetic ferromanganese crusts (Bau and Koschinsky, 2009), during weathering (Land et al., 1999), and between chert, iron oxide and carbonate minerals in the Abitibi Greenstone Belt (Baldwin et al., 2011). Here we use an optimized sequential extraction scheme to examine the three main mineral fractions in the Asbestos Hills IF: Fe-carbonates (ankerite and siderite), magnetite (as hematite is a trace mineral or absent) and the Fe-silicates (greenalite, minnesotaite, riebeckite and stilpnomelane) plus chert (Oonk et al., 2017). We assess and verify the sequential extraction method against mineral-specific LA-ICP-MS analyses, and bulk-rock mineralogy and chemistry from the same rocks. We then apply our methodology to study pre-GOE seawater REE variability in Transvaal

Supergroup rocks of the Paleoproterozoic Griqualand West Basin, South Africa. Our work represents an important step forward in quantitatively comparing REY patterns in IF carbonates with co-existing oxides and silicates.

2. REE SYSTEMATICS IN IRON FORMATIONS

Ionic radii show a gradual decrease from La (1.18 Å) to Lu (0.97 Å) (Haynes, 2017) as a result of progressive filling of the 4f electron orbital. This results in predictable and progressive variability in the abundance of REE versus atomic number in most geochemical systems. Anomalous behaviour of individual elements can be quantified by dividing the measured abundance of an element by one extrapolated from the neighbouring REE, denoted as $[REE_n/REE_n^*] = REE_n/(½REE_{n-1}+½REE_{n+1})$, where REE_n is the normalized elemental abundance and n is an integer and represents the element in question in the order of the lanthanide series (Bolhar et al., 2004). Estimation using this method becomes more difficult when an element has only one REE of adjacent mass, or if a neighbouring element potentially behaves anomalously as well. Both La and Ce can be anomalous in IF and since La is the lowest mass REE, La and Ce anomalies are best expressed graphically by plotting Ce/Ce^* vs. Pr/Pr^* (Bau and Dulski, 1996). The La anomaly can also be quantified by extrapolating from Nd and Pr as La/(3Pr-2Nd) (Bolhar et al., 2004). Since adjacent Eu and Gd can both be anomalous in IF, their variance is calculated by extrapolating between Sm and Tb: $[Eu/Eu^*] = Eu/(⅔Sm + ⅓Tb)$ and $[Gd/Gd^*] = Gd/(⅓Sm + ⅔Tb)$ (Bau and Dulski, 1996).

Cerium and Eu are the only REEs with additional oxidation states in nature next to the standard trivalent one. The (microbial) oxidation pathways of Ce and Mn are closely linked and are not simple functions of pH, oxygen concentration or other physical parameters (Moffett, 1994). Thus, although the standard electrode potentials for Ce oxidation are higher than for Mn oxidation ($E°$ (V) = +1.72 vs. +1.54 at 25 °C; Haynes, 2017) under most Eh-pH conditions, Mn can still be in its divalent form when Ce is oxidized to the tetravalent state (e.g. Nakada et al., 2016). The modern negative Ce anomaly in seawater is linked to scavenging of Ce(IV) onto Mn-nodules/particulates (e.g. Elderfield et al., 1981). Therefore the absence of a negative Ce anomaly in seawater-like patterns captured by many pre-GOE IFs (e.g. Bau and Dulski, 1996; Alexander et al., 2008; Frei et al., 2008; Planavsky et al., 2010) indicates that the seawater was still reducing enough to prevent the formation of Mn-oxides.

Positive Eu anomalies in chemical sediments indicate a strong influence of hydrothermal fluids on the seawater Eu concentration (Dymek and Klein, 1988; Klein and Beukes, 1989; Bau and Dulski, 1996; Bolhar et al., 2004). Under high-temperature (>250 °C) and low Eh, hydrothermal extraction of divalent Eu is more efficient than for other trivalent REEs (Bau and Möller, 1993). The hydrothermal fluid will therefore contain a positive Eu anomaly, which under anoxic conditions will influence the seawater budget (Bau and Möller, 1993; Bau and Dulski, 1996). Positive Eu anomalies are present in most IFs (e.g. Planavsky et al., 2010), however they are absent in IFs deposited in association with "Snowball Earth" conditions (e.g. Tsikos and Moore, 1997; Halverson et al., 2011).

The usefulness of inserting Y between Dy and Ho, based on its ionic radius, has been shown before in IFs (e.g. Bau and Dulski, 1996; Delvigne et al., 2012). In present day seawater, Y behaves anomalously compared to Ho, which has geochemical similarities based on charge and radius (Bau, 1996). This behaviour has been attributed to surface complexation effects, where differences in type of chemical bonding (covalent vs electrostatic) signify that Y binds less strongly as surface-complexes compared to REEs. As a result, Y is less prone to removal from seawater, creating superchondritic Y/Ho ratios in the contemporary oceans (Bau, 1996). Superchondritic Y/Ho ratios in IF have therefore been interpreted as a primary seawater signature (e.g. Bolhar et al., 2004), however, small positive Y anomalies have been shown to arise in river waters due to the preferential loss of Y over Ho during silicate weathering (Lawrence et al., 2006: Babechuk et al., 2015).

3. SAMPLES AND METHODS

3.1. Regional geology

Deposition of large-scale IFs culminated around the GOE at ca. 2.4 Ga. At that time the large Krivoy Rog-Kursk, Cauê, Hamersley and Transvaal IFs were formed (Bekker et al., 2010; Konhauser et al., 2017). Direct correlation between the latter two iron formations remains open for debate. However, recent age dating correlates the Kuruman IF (2460 ± 5 Ma; Pickard, 2003) to the Brockmann and the Weeli Wolli IFs in the Hamersley basin (Trendall et al., 2004; Kampmann et al., 2015; Gumsley et al., 2017). The Brockman Formation consist of two major IFs, the 2.48 Ga Dales Gorge member and the 2.46 Ga Joffre member (Trendall et al., 2004). The overlying Weeli Wolli IF is slightly younger with an age of 2.45 Ga (Barley et al., 1997). The Griquatown Formation has been correlated with the lower Boolgeeda IF (Beukes and Gutzmer, 2008; Kampmann et al., 2015).

The Transvaal Supergroup was studied in the northern part of the Griqualand West basin (Fig. 1). In this area a large, thick carbonate platform (Campbellrand-Malmani) was developed prior to IF deposition, which thins out going to the southern parts (e.g. Beukes and Gutzmer, 2008). The top of the Campbellrand Subgroup, the stromatolitic Gamohaan Formation, has been used to argue for the presence of oxygen-producing cyanobacteria based on N-isotope evidence (Godfrey and Falkowski, 2009). The transition into the Asbestos Hills Subgroup is continuous and indicates a deepening of the basin from the stromatolites to the micro-banded IFs of the Kuruman Formation (Klein and Beukes, 1989; Sumner, 1997). The rhythmically banded IF (BIF) of the Kuruman Formation was largely deposited in an open-shelf environment below wave base and contains multiple cycles of shallowing upward sequences (Beukes, 1984). Multiple sedimentological members have been described in the Kuruman Formation, based on outcrops in the southern part of the Griqualand West

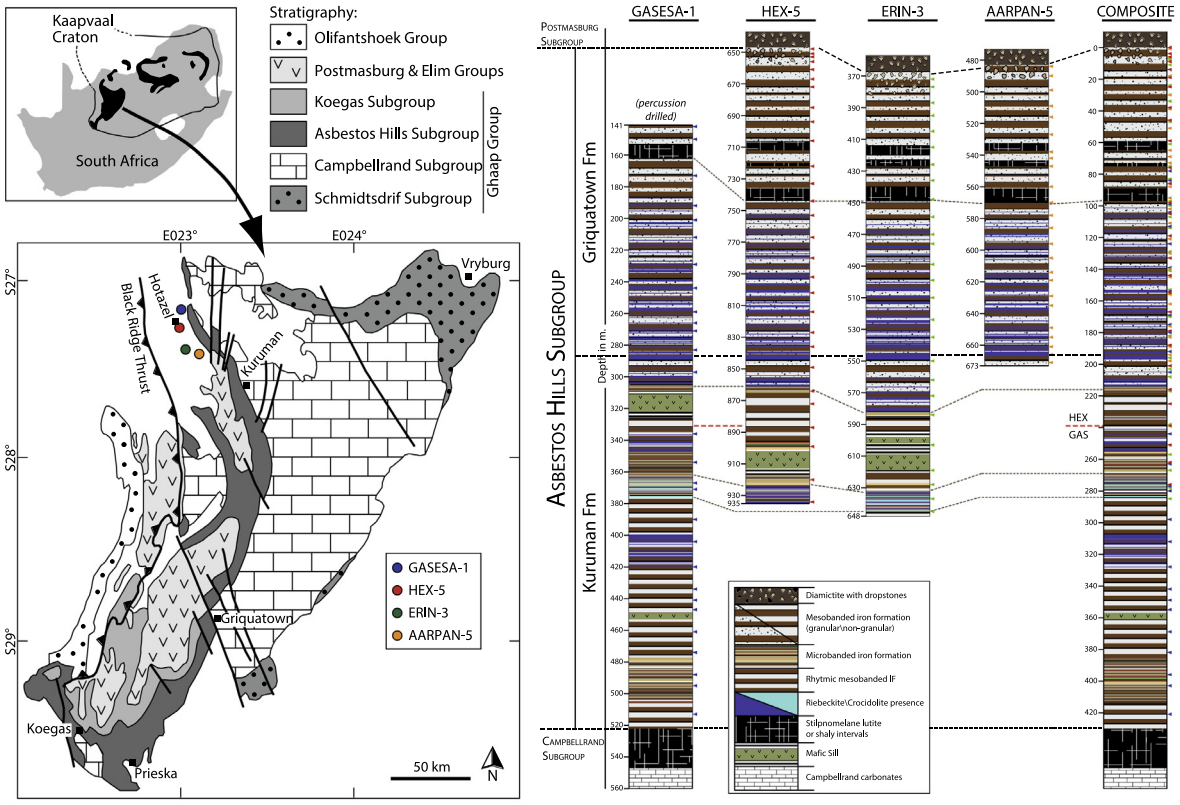

Fig. 1. Regional geology of the Griqualand West Basin in the Kaapvaal Craton (modified from Schröder et al., 2011; Oonk et al., 2017) showing the locations of the drill cores selected for this study, their respective schematic logs and the composite log based on the HEX and GAS cores. Arrows drawn next to the columns represent places where the samples were taken. The sample depths in the composite log were recalculated based on multiple marker beds within the different cores.

basin (Beukes, 1984). They are difficult to distinguish in drill core-sections from the top of the carbonate platform where the Kuruman Formation is only ca. 200 m thick.

A SHRIMP U/Pb zircon age based on stilpnomelane-rich tuffaceous mudrocks, dates the Kuruman IF at 2460 ± 5 Ma (Pickard, 2003). The Kuruman IF is interrupted by two basaltic andesitic sills, a thinner one (3 m thick) in the lower mesobanded part and a thicker interval near the Kuruman-Griquatown transition. The IFs immediately around these sills are carbonate depleted due to contact metamorphism. The transition from the Kuruman to the Griquatown is in itself intriguing, since transitions from microbanded to granular IFs are uncommon (Beukes and Klein, 1990). The Griquatown IF has been dated at 2431 ± 31 Ma (zircon U–Pb SHRIMP age; Trendall et al., 1990) and its thickness varies between 200 and 300 m (Oonk et al., 2017). The clastic texture in the Griquatown Formation is clear, with soft-sediment deformation features, chert pods, granules of varying composition in the same bed and even well sorted grainstones, indicating a shallower-water, storm-dominated depositional environment (Beukes, 1984; Beukes and Klein, 1990; Beukes and Gutzmer, 2008). The central part of the Griquatown IF consists of three, thick, laterally continuous stilpnomelane lutites. These lutites are interpreted to represent volcanic ash beds (Beukes, 1984) and might be correlated to the shale-macrobands in the Hamersley basin (e.g. Beukes and Gutzmer, 2008). Wind-blown ashes could have been derived from the 'Hamersley' arc-retro arc system located at the southern margin of (Zim)vaalbara (Zeh et al., 2016).

In the south-western part of the Griqualand West Basin, the Koegas Subgroup overlies the Griquatown Formation, however the Koegas is absent in our study area. Here, the Griquatown Formation is directly overlain by the Makganyene diamictite. The basaltic-andesitic Ongeluk volcanics are deposited on top of the Makganyene Formation, which in turn are overlain by youngest IF present in the Griqualand West Basin, the Hotazel Formation (e.g. Tsikos and Moore, 1997, Tsikos et al., 2003; Lantink et al., 2018). Throughout large parts of the Hotazel Formation the main Fe-oxide is hematite, in contrast to the magnetite in the Asbestos Hills IFs. This, in combination with the presence of thick Mn-oxide ores indicates deposition syn- or just post-GOE for the Hotazel Formation (Tsikos and Moore, 1997, Tsikos et al., 2003; Lantink et al., 2018).

3.2. Sampling strategy

The Kuruman and Griquatown IFs were sampled from four drill-cores: Gasesa-1 (GAS), HEX-5 (HEX), Erin-3 (ERI) and Aarpan-5 (ARP), which cover a ca. 25 km NW-SE trajectory near the town of Hotazel (Fig. 1). The

cores were drilled as part of a water exploration-programme in the mid-1990′s and stored in the South32 core yard in Hotazel. The top of GAS was percussion drilled and therefore the contact between the IFs and the Makganyene diamictite is missing. This core captures most of the Griquatown, the entire Kuruman and part of the Gamohaan Formations. The HEX and ERI cores capture part of the Kuruman IF, whereas the ARP core stops around the Griquatown-Kuruman transition. However, these last three cores capture the Griquatown-Makganyene contact. The cores were correlated using marker-beds and a composite log was made through ca. 430 m of IF-stratigraphy (Fig. 1). Samples were taken circa every 15 m for the GAS, 10 m for the HEX and ERI and 7 m for the ARP cores. They consisted of 5–15 cm half-core fragments, capturing the diversity of IF, giving a total of 101 IF samples and 5 lutite samples (Fig. 1). No samples were taken within a few meters of the mafic sills present in the Kuruman Formation. Samples are labelled by their core-abbreviation (GAS, HEX, ERI, ARP) followed by their depth in meters.

3.3. Analytical techniques

Thin sections were made for each sample. The offcuts were crushed and then pulverized using a tungsten carbide swinging mill, followed by at least 30 min in an automated agate pulveriser to create a very fine-grained powder. Bulk-rock sample characterization took place at Rhodes University, where the chemical composition was determined by x-ray fluorescence spectrometry (XRF), and mineralogy was resolved by optical microscopy and x-ray diffraction (XRD). Minor and trace element concentrations were determined by inductively coupled plasma-mass spectrometry (ICP-MS) at Utrecht University after a standard bulk-rock digestion procedure using HF-$HClO_4$-HNO_3 (5:3:2).

Chemical separation of the samples was carried out using a recently-developed sequential extraction procedure (Oonk et al., 2017). In summary, 30–50 mg of powdered sample was transferred into a 15 ml Greiner© tube. Each extraction used 10 ml of reagent, and after each step the sample was centrifuged and the supernatant filtered (0.2 µm). The extraction was started with 1 M Na-acetate

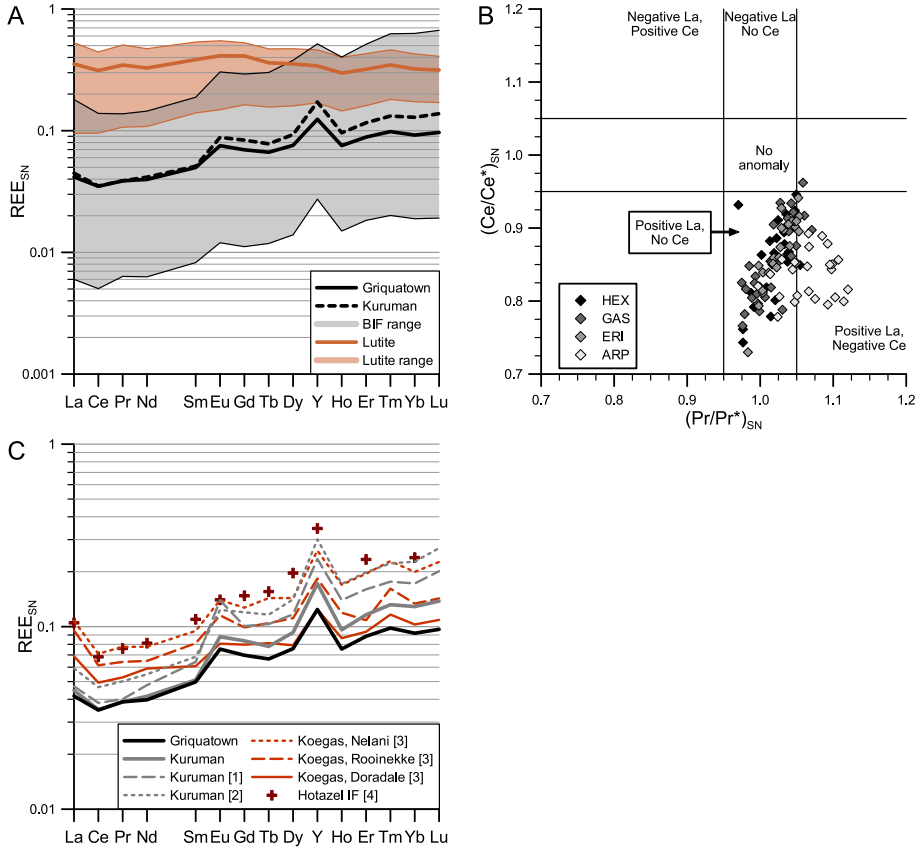

Fig. 2. Bulk-rock rare earth element plus yttrium (REY) data. (A) Bulk-rock REY_{SN} ranges (light shaded fields) and averages (solid lines) for IF (grey) and lutite (brown; n = 5) samples. The IF averages are shown for the Kuruman (n = 34) and Griquatown (n = 67) formations. (B) $(Ce/Ce^*)_{SN}$ vs $(Pr/Pr^*)_{SN}$ for samples from the Kuruman and Griquatown formations showing La and Ce anomalies as defined by Bau and Dulski (1996). (C) Average Griquatown and Kuruman IF data of panel A compared to averaged literature REY_{SN} data of the Transvaal IFs. Kuruman data are from [1] Bau and Dulski (1996; n = 14) and [2] Planavsky et al. (2010; n = 3; note that here are Gd data absent). Koegas data from [3] Nel (2013), where flat lutite patterns were excluded for averaging. Koegas data include Nelani IF (n = 20), Rooinekke IF (n = 10) and Doradale IF (n = 7). Hotazel IF data [4] from Tsikos and Moore (1997; n = 12; note that Ho, Tm and Lu are absent).

(pH adjusted with acetic acid to 4.5) under an inert N_2 atmosphere and allowed to react for 48 h at 50 °C in a shaking incubator. The acetate step targeted the carbonates, with duration and temperature optimized for the extraction of crystalline siderite (Poulton and Canfield, 2005). Subsequently, a digestion step in 0.2 M NH_4-oxalate/0.17 M oxalic acid was applied for 24 h, to extract the magnetite and any minor amounts of hematite present. The final residue was transferred to PFA-vials (Savillex, USA) for digestion using HF-HNO_3-$HClO_4$, targeting the silicate minerals.

Rare earth element and trace element distributions were determined by ICP-MS (Thermo Scientific X-series 2) at Utrecht University. Calibration standards were matrix-matched to avoid suppression/enhancement effects and calibration curves were weighted (weighing factors of 1/concentration) to account for the concentration range that covered several orders of magnitude. A 10 ppb In-spike was used for internal standardization to correct for intra-run drift. Data are reported only above the element specific limit of quantification (LOQ), calculated as 10x the standard deviation of 10 blank, matrix-matched samples. Blank subtraction was calculated independently within each run.

To determine REE distribution among the various minerals, mineral-specific REE patterns were measured using a 193 nm wavelength COMPex 102 ArF excimer laser ablation system (Lambda Physik) connected to an Element 2 sector field ICP-MS (Thermo Scientific) at Utrecht University. The mass spectrometer was operated in low-resolution mode. Laser ablation was performed with an energy density of 10 J/cm^2 and a pulse repetition rate of 10 Hz. The spot size (80 μm) was optimized to provide low detection limits for the REE but this prevented measurement on small grains. ^{56}Fe was used as an internal standard for all minerals, except ankerite where ^{43}Ca was used. Data reduction was performed using the GLITTER software. Calibration was performed against NIST SRM 612. Reference material BCR-2G was used as a secondary standard, with results typically within 20% of published reference values taken from the GeoReM database (Jochum et al., 2005). At least four individual grains of the target minerals were analysed in every thin section. The purity of each grain was evaluated offline, by comparing the major element abundances to pure mineral data. The Si concentration could not be used to evaluate purity, because very fine-grained chert was present in all samples. The filtered results (n = 1–6) per mineral were then averaged for each sample. All REE (and REY) patterns were normalized to Post-Archean Australian Shale (PAAS) using the values of McLennan (1989). Normalization to PAAS is common convention and thus used here, but suspected erroneous values for Tm reported in PAAS can lead to apparent Tm anomalies (e.g. Fig. 2) that are unlikely to be real (Kamber et al., 2005).

4. RESULTS

4.1. Bulk-rock analysis

PAAS-normalized bulk-rock REY data show a clear distinction between lutite and IF samples (Fig. 2a; full data tables given in supplementary data repository). The lutites show generally an unfractionated flat pattern, i.e. shale-like, whereas the IFs tend to be heavy REE (HREE) enriched. The average Y/Ho ratio is super-chondritic for the IF samples (45.2 ± 6.1), but close to chondritic for the 5 lutite samples (29.5 ± 2.0). Bulk-rock Ce anomalies are generally absent whilst La shows predominantly positive anomalies (Fig. 2b), confirming previous work on Paleoproterozoic IFs (e.g. Bau and Dulski, 1996; Bolhar et al., 2004; Planavsky et al., 2010). Some of the ARP samples show an apparent negative Ce anomaly. This was only observed in a limited number of bulk rock results and not reproduced by the fraction-specific or mineral data from the same samples and is thus likely to represent an analytical artefact in these few bulk-rock analyses. An absence of Ce anomalies generally indicates that the seawater is still reducing with respect to Mn (Bau and Dulski, 1996). Even for the Hotazel Formation, in the Postmasburg Subgroup, and possibly deposited during or after the GOE (Gumsley et al., 2017), a clear negative Ce anomaly remains largely absent (Tsikos and Moore, 1997), possibly present only in a single analysis of braunite lutite (Bau and Alexander, 2006). These trends match those found previously for bulk-rock Transvaal IFs of the Kuruman (Bau and Dulski, 1996; Planavsky et al., 2010), Koegas (Nel, 2013) and Hotazel Formations (Tsikos and Moore, 1997). The bulk-rock samples of Bau and Dulski (1996) came only from the lower half of the Kuruman BIF (Groenwater member). The stratigraphic location of the three samples from Planavsky et al. (2010) is not disclosed and Gd data are missing. The strong Eu anomaly present in the Kuruman data of Bau and Dulski (1996) is less obvious in the other averaged patterns (Fig. 2c). Age equivalent bulk-rock samples from the Dales Gorge IF in the Hamersley basin (Pecoits et al., 2009; not shown here) have similar features.

Supplementary data associated with this article can be found, in the online version, at https://doi.org/10.1016/j.gca.2018.07.005.

4.2. Mineral-specific analysis

Grain-specific REY patterns of the different IF minerals are plotted in Fig. 3 (data in supplementary tables). Averaged data show positive Eu and Y anomalies and positive La anomalies are present in all minerals except magnetite and riebeckite. The positive slope in carbonate minerals matches those found in Dales Gorge IF carbonate minerals (Alibert, 2016) and is similar to the slope of present day seawater (Alibo and Nozaki, 1999). Although there is some scatter in the silicate data, most of the patterns are HREE enriched. The stilpnomelanes with the highest total REE tend to have more unfractionated LREE/HREE. The steepest REE slopes present are those of the amphibole-mineral riebeckite. Although the Eu anomaly in the data from Alibert (2016) tends to be more pronounced, the patterns for magnetite, greenalite and minnesotaite are quite similar. However, the Dales Gorge magnetite and minnesotaite are more depleted in LREE (La-Nd) than those we report here.

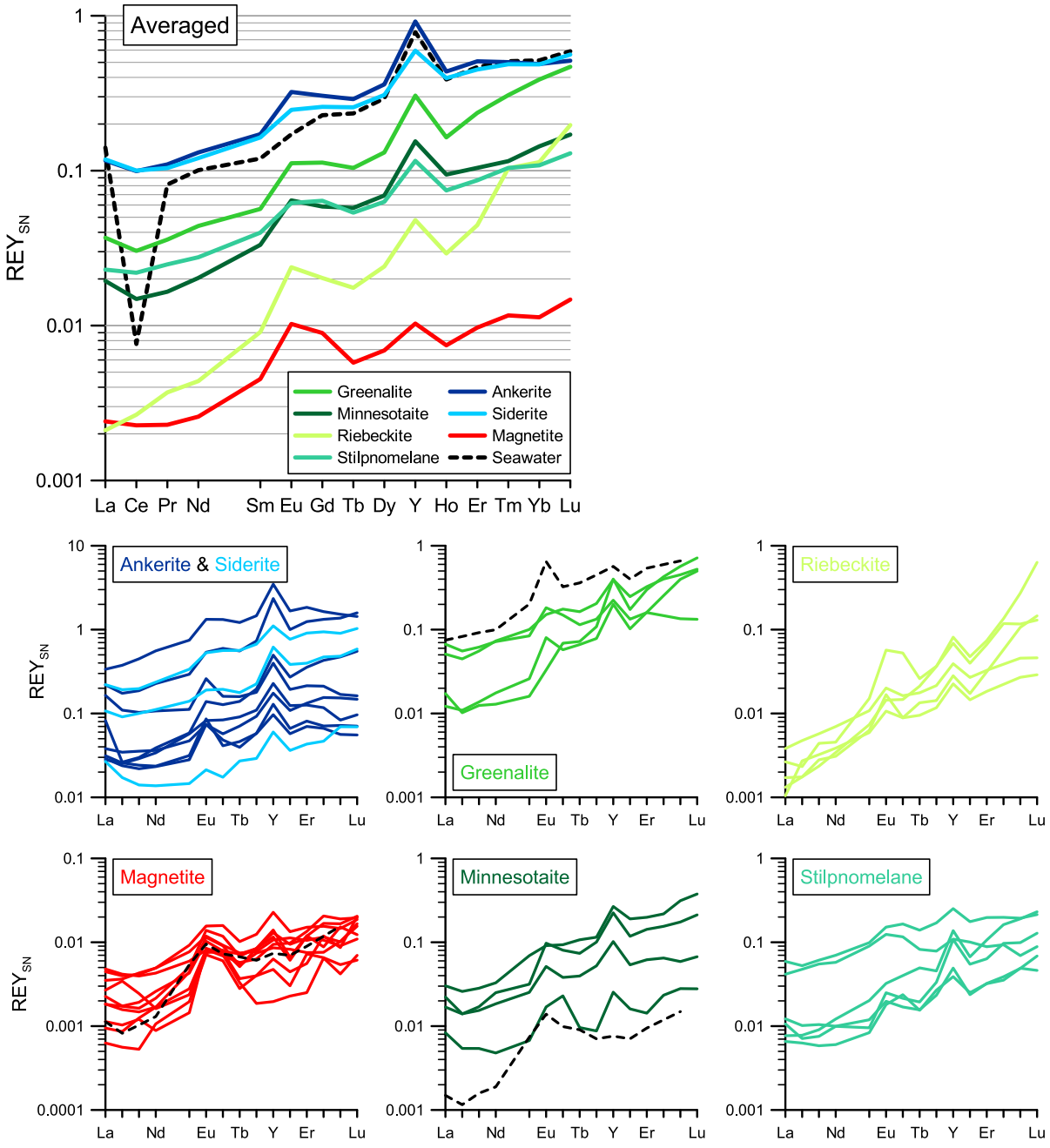

Fig. 3. Average REY_{SN} patterns of minerals from the Asbestos Hills IFs. The patterns of the individual minerals are averages of 1–6 different grains within a single thin section, the black dotted lines shown in the specific mineral data panels are average (greenalite, minnesotaite: n = 1 and magnetite: n = 11) patterns found in Hamersley IFs (Alibert, 2016). The present day seawater curve (*10^6) in the averaged diagram is from the North Pacific Deep Water at 2500 m (Alibo and Nozaki, 1999).

4.3. Fraction-specific REY analysis

4.3.1. Recoveries and reproducibility

The recoveries (summed fractional data versus bulk-rock data) for iron and other major elements are excellent (shown in more detail in Oonk et al., 2017). For the REE, the calculated recoveries are similar (Fig. 4a) and lie between 75 and 120%, which is within the standard error for sub-ppb measurements by ICP-MS. The median recovery for Eu is slightly poorer than the other REE, with a value of 80%. In-house quality control standards (QC) and standard reference material results show that bulk-rock measurements overestimate Eu by ca. 10%, and species-specific QC values show an underestimation of ca. 20%. The measured ^{153}Eu values could have been influenced by Ba-oxide interferences (Jarvis et al., 1989), but no systematic offset was found when comparing Ba concentrations and corresponding Eu data. The average Ba/Eu

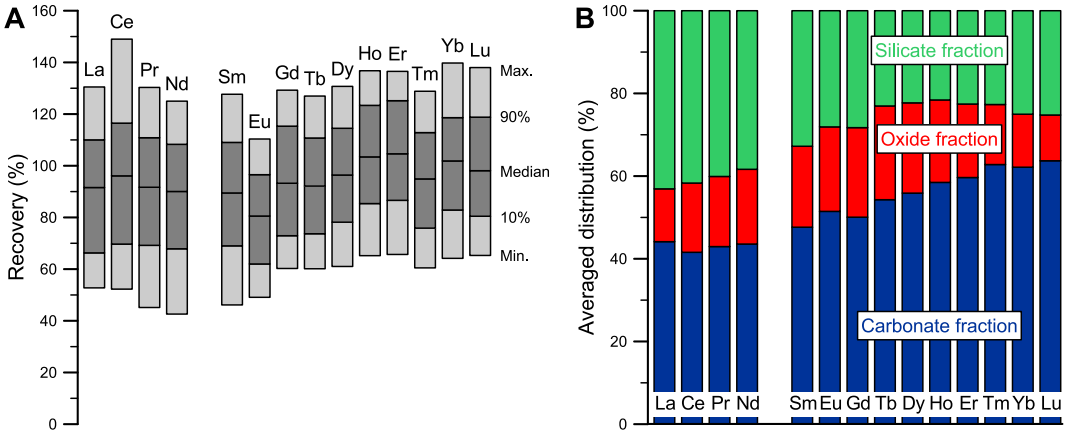

Fig. 4. Sequential extraction data for the Asbestos Hills IFs. (A) Recovery values of the REEs calculated from summed fractional data versus bulk-rock data. The median and the range for all samples are shown. (B) The average Asbestos Hills IF sample-specific REE distribution over the three extracted fractions. This was calculated by determining the distribution per sample, then averaging over all samples.

ratio (ca. 236) in the measured samples is within the same order of magnitude as the calibration standards (110) and unlikely to have induced significant uncertainties on the Eu data. Even when 5% of the measured Ba would have been converted to BaO^+, which is higher than typical values (ca. 1–2%, Jarvis et al., 1989), the effect on the QC recovery rate of Eu would only have been minor (3% increase). Thus the slightly poorer quality of the Eu-data is unlikely to be related to Ba-interferences, but interpretation of the data should still be treated with caution. Nonetheless, the Eu anomalies described previously for the Kuruman BIF (Bau and Dulski, 1996; Planavksy et al., 2010) are higher than the ones found here, whereas the average Koegas IF patterns (Nel, 2013) are similar (Fig. 2c).

The averaged distribution of the specific REEs per sample are shown in Fig. 4b. The acetate and HF fractions show an antithetic relationship, where the silicates are dominated by LREE and the carbonates by HREE. Although generally REE-poor, the oxalate fraction is relative enriched in middle REE (MREE). Two samples, GAS722 and HEX836, were reproduced as 8 separate digestions and showed excellent agreement for the REY patterns (Fig. 5), with very good reproducibility of absolute concentrations (see online supplement). The reproducibilities of Gd and Tb are slightly poorer in the silicate fraction. For the other duplicate samples, the reproducibility lies generally within the typical uncertainty at the tens of percent level of the ICP-MS measurements. From here on replicate values were averaged per sample.

4.3.2. Distribution and general overview

To directly compare fraction-specific REY patterns with each other and with mineral-specific data, they have to be normalized to the percentage of that fraction within the bulk-rock. Each normalization factor was calculated based on the amount of major oxides extracted (plus bulk-rock CO_2 for the acetate). Fractions consisting of less than 10 wt% were omitted because of their large uncertainties due to the low REY-abundances in combination with high normalization factors (Oonk et al., 2017).

In addition to the five Griquatown lutite samples, the remaining 101 IF samples were taken from the Kuruman (n = 34) and Griquatown (n = 67) Formations. After filtering the dataset for LOQ and the 10 wt% cut-offs, 92 acetate, 67 oxalate and 100 HF samples were accepted and have complete REY patterns. The 92 acetate samples constitute

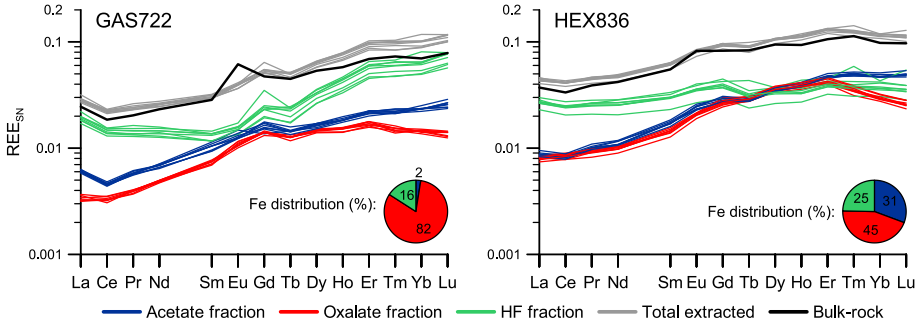

Fig. 5. Species specific REE_{SN} patterns of GAS722 and HEX836 measured in 8-fold. The reproducibility is generally good and the calculated total values (grey line for each replicate) closely match their measured bulk-rock values (thick black lines). Pie-charts show the Fe-distribution in each sample. The anomalously high Gd value for the HF fraction in GAS722 is most likely related to analytical error, as the other elements in that run were similar to their duplicates. See the text for the discussion on the Eu anomaly.

25 Kuruman samples, 63 Griquatown IF samples and 4 Griquatown lutites; for the 67 oxalate samples these numbers were 27, 39 and 1 respectively, and the 100 HF-samples were split as 32, 63 and 5 respectively. These cut-off criteria reflect the fact that the Kuruman samples were relatively magnetite-rich (27 accepted of the 34 samples) and the Griquatown samples were magnetite-poor (39 of the 67).

The REY_{SN}-ranges of the IF and lutite samples are plotted in Fig. 6a–c together with the averages for the Kuruman and Griquatown samples. The acetate fraction shows a relatively narrow range in normalized-abundance relative to the other fractions (Fig. 6a) and all samples have a positive slope. The oxalate-extracted REY_{SN} patterns show a MREE enrichment relative to the Pr-Yb line from Eu to Er (Fig. 6b, Section 5.3). The largest range is found in the silicate fraction (Fig. 6c) which varies over three orders of magnitude. This variation can be explained by sample-specific silicate mineralogy as well as variable dilution with chert.

The Y/Ho ratios seen in the bulk IF and lutite samples are also recorded in the different fractions, i.e. superchondritic ratios for IF and near chondrite values for the lutites. The positive La anomaly present in the bulk-rock samples is absent in the oxalate fraction (Fig. 6d). The La anomaly is most pronounced in the carbonate fraction, which averages around the bulk-rock mean. The extent of the La anomaly varies with stratigraphy, it is much more pronounced in the Kuruman than in the Griquatown carbonate fraction (Figs. 6a and 7c–d). The silicate fraction plots between the oxalate and carbonate fractions. These anomalies are consistent in the LA-ICP-MS data, as magnetite and riebeckite are the only minerals without a positive La anomaly (Fig. 3).

The Griquatown IF samples are enriched in LREE and depleted in HREE compared to the Kuruman samples, in both the bulk-rock and all three fractions. This can be constrained by $(Yb/Pr)_{SN}$, which was chosen since both elements lack anomalous behaviour and span most of the range in atomic mass of the REEs (e.g. Bolhar et al., 2004). In the acetate fraction, $(Yb/Pr)_{SN}$ decreases stratigraphically from a mean value of 8.0 in the Kuruman Formation to 3.9 in the Griquatown IF (Fig. 7). This decrease is less pronounced in both oxalate (3.9–2.6) and HF (2.6–2.1) fractions (not plotted in the figure). For the bulk-rock samples the average $(Yb/Pr)_{SN}$ in the Kuruman (3.7) decreases to 2.5 for the Griquatown IF. Stratigraphic changes in $(Yb/Pr)_{SN}$ seen in the carbonate fraction correspond to a shift in the magnitude of the La anomaly (calculated as either Ce/Ce^* or La/La^*), but without any change in $(Y/Ho)_{SN}$ (Fig. 7).

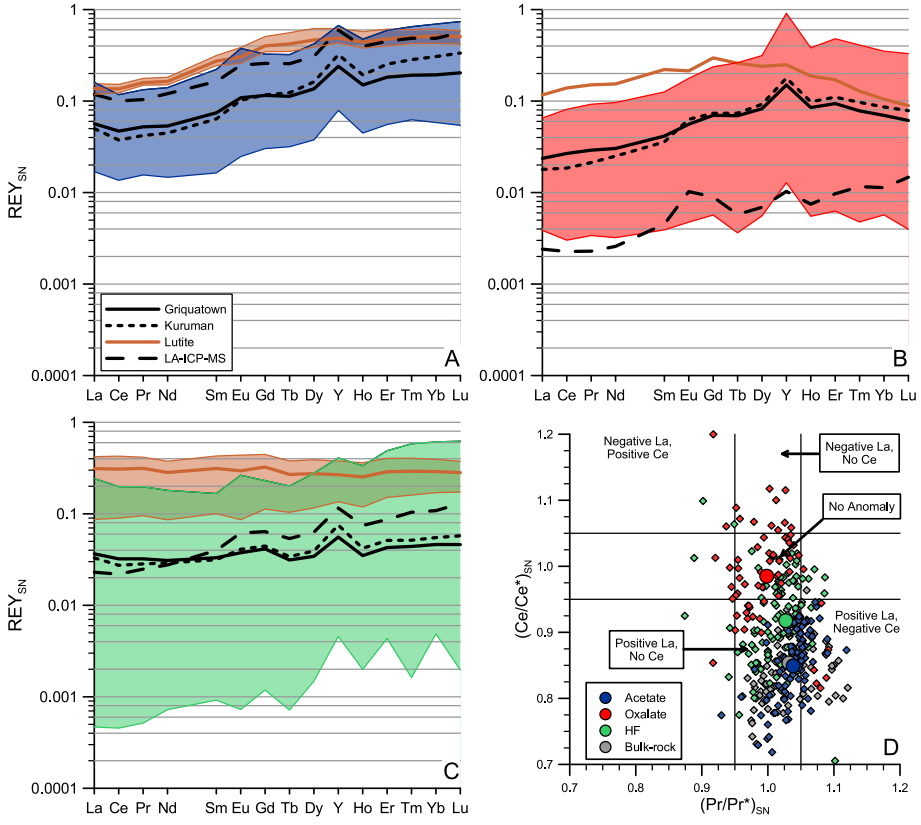

Fig. 6. Fraction-specific REY_{SN}-ranges for the (A) acetate, (B) oxalate and (C) HF extractions. Solid and dotted lines are the means for the Griquatown and Kuruman samples respectively. Brown lines and ranges are for the lutite sample(s). The dashed LA-ICP-MS line is the mean siderite (panel A), magnetite (panel B) and stilpnomelane data (panel C). D: $(Ce/Ce^*)_{SN}$ vs $(Pr/Pr^*)_{SN}$ showing fraction-specific La and Ce anomalies as described in Bau and Dulski (1996). The round symbols are the means of the fractions, the colored diamonds represent individual samples.

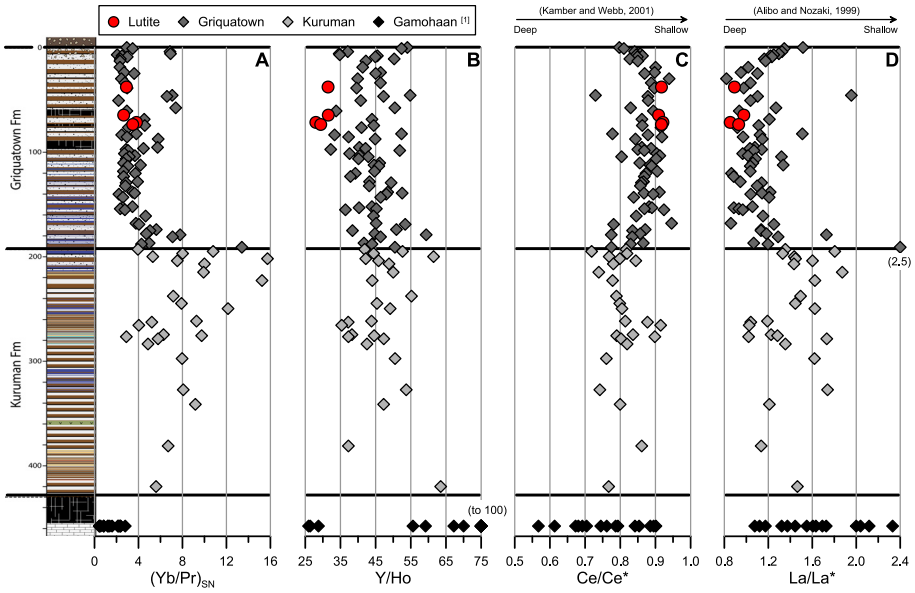

Fig. 7. Acetate extracted REY signatures versus stratigraphic depth in the Asbestos Hills IFs. (A) $(Yb/Pr)_{SN}$, (B) Y/Ho, (C) shale-normalized Ce/Ce^* ($Ce^* = \frac{1}{2}La + \frac{1}{2}Pr$), (D) shale-normalized La/La^* ($La^* = 3Pr\text{-}2Nd$). Differences between the Kuruman and Griquatown formations are clear in panels A, C and D, whereas the Y/Ho ratios remain relatively constant. The lutite Y/Ho are close to chondrite values (See text for discussion). Data for the Campbellrand (Gamohaan) carbonates was taken from Kamber and Webb (2001).

5. DISCUSSION

5.1. Bulk rock REY

Bulk rock REY data can be affected by contamination through detrital input (e.g. Bau and Möller, 1993) and/or volcanic ash (e.g. Thurston et al., 2012), even in distal marine settings. Minor amounts of addition of REE-rich shales (<1 wt%) to BIF or chert have been shown to have a strong influence on REE slope (e.g. Bau, 1993; Webb and Kamber, 2000; Van Kranendonk et al., 2003). Cherts might also represent silicified zones of precursor felsic volcanic ash (Thurston et al., 2012). The Asbestos Hills subgroup samples show highly variable $(Yb/Pr)_{SN}$ but with a shift from higher values in the deeper-water Kuruman to lower ones in the shallower Griquatown IF. This may reflect an increasing role for input of terrigenous material with changing water depth and proximity to the margin of the basin. We have tested this by comparing REE data against chemical indicators for clastic contamination such as the immobile high field strength (HFSE) elements Zr, Ti, Hf, Th and Sc (Bau, 1993; Viehmann et al., 2015). Zirconium shows a correlation against Nd for the bulk-rock Asbestos Hills samples and indicates that detrital contamination has influenced bulk rock REE variability (Fig. 8a). Neodymium was selected since it reflects the enrichment in LREE that are typically most affected by allochthonous material (Viehmann et al., 2015). Corresponding changes in $(Yb/Pr)_{SN}$ also track Zr abundance (Fig. 8b). The samples from Bau and Dulski (1996) are relatively elevated in $(Yb/Pr)_{SN}$, but also show a similar correlation against Zr. The lutite samples we measured here contain the highest concentrations of REE and HFSE elements, but have been suggested to reflect input from volcanic ash (Beukes, 1984) rather than detrital sources. If the most enriched lutite was close to a detrital or ash end-member, then we reach an estimate of up to 10% allochthonous material required to explain the majority of the bulk-rock REE variability in the IF samples (Fig. 8). This likely represents an upper estimate for contamination as other allochthonous inputs might have been more enriched in trace elements. Previous work has shown similarities between Kuruman REY plots and modern seawater suggesting minimal or no input of contaminant material (Bau and Dulski, 1996) (Fig. 9). However, we argue that a small effect of contamination is difficult to resolve. Other studies that show apparent similarities between bulk rock IF REY patterns and seawater might be also affected to a small degree by terrestrial material or volcanic ash input (e.g. Derry and Jacobsen, 1990).

5.2. Carbonate fraction

Measurement of REE in the carbonate fraction avoids the control of detrital/volcanic ash input on abundance variations, since these contaminants should not be extracted by the acetate digestion. The carbonate fraction-normalized Zr concentration for our Asbestos Hills samples is generally well below 1 ppm, indicating that the majority of the bulk rock data are contaminated to some extent. The lack of a correlation between $(Yb/Pr)_{SN}$ and Zr in the carbonate fraction indicates negligible allochtonous input in this fraction (Fig. 8c). Carbonate mineralogy can be constrained by the Ca concentration in the acetate fraction since siderite is Ca-free, calcite only exists as a trace mineral and the Ca/Fe ratio in ankerite is relatively constant. The lack of a correlation between Ca and $(Yb/Pr)_{SN}$ (data not plotted here) indicates that the REE slope change is independent of carbonate mineralogy. Stratigraphic

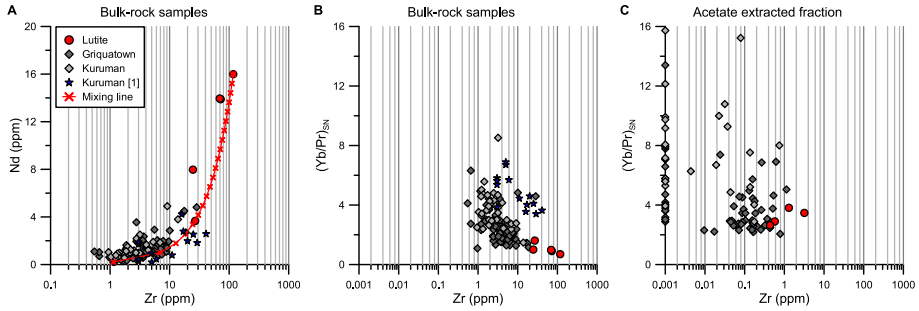

Fig. 8. (A) Bulk-rock Nd (ppm) versus Zr (ppm) concentrations in the Asbestos Hills IFs. The lutite sample (red dots) with the highest Zr and Nd concentration was taken as a modelled contaminant and the lowest concentration sample as the pure BIF component. The crosses on the mixing line represent a 5% increase in detrital or volcanic ash contaminant, suggesting that most BIF samples contain less than 10% allochtonous material. (B) Bulk-rock and (C) acetate extracted $(Yb/Pr)_{SN}$ versus Zr, respectively. See text for discussion. For the acetate extracted fraction, numerous samples had Zr concentrations below detection limit and to give an overview their $(Yb/Pr)_{SN}$ values are plotted on the y-axis. Additional Kuruman bulk-rock values [1] from Bau and Dulski (1996), where in case of Zr concentrations <5 ppm an arbitrary concentration of 3 ppm was assigned to allow plotting. Note the horizontal scale change between (a), and (b) and (c). (For interpretation of the references to colour in this figure legend, the reader is referred to the web version of this article.)

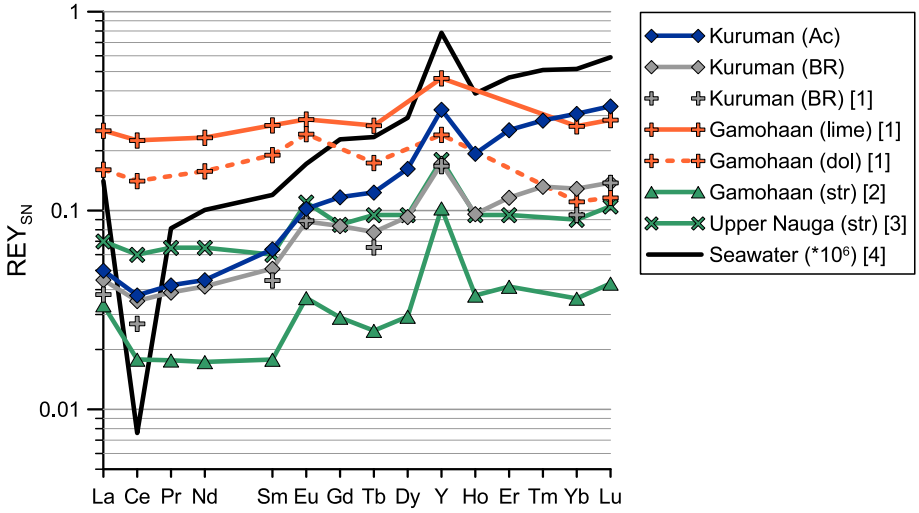

Fig. 9. REY_{SN} patterns of the Kuruman and Gamohaan Formations showing the averages of the acetate-extracted fraction (Ac), bulk-rock data (BR) of the Kuruman, the Gamohaan carbonates (limestone (lime), dolomite (dol) and microbial carbonates (str)) and the modern seawater composition ($*10^6$). Note that the Griquatown acetate-extracted fraction (not shown here- see Fig. 6a) resembles the Kuruman data and its $(Yb/Pr)_{SN}$ is even closer to modern seawater. Data from: [1] Klein and Beukes (1989); [2] Kamber and Webb (2001); [3] Voegelin et al. (2010) and [4] Alibo and Nozaki (1999).

variations in carbonate fraction $(Yb/Pr)_{SN}$ are thus likely to reflect changes in REE source and/or variable fractionation in the sediment during diagenesis or in the primary water column. Water column variations in LREE/HREE are observed in present day oxidized seawater, with changes in slope typically seen with depth (e.g. Piepgras and Jacobsen, 1992; Alibo and Nozaki, 1999). Our extracted carbonate fraction REY data have closer to modern seawater $(Yb/Pr)_{SN}$ values than the bulk rock measurements on the same samples (Fig. 9). The average $(Yb/Pr)_{SN}$ values of modern seawater vary between 2.4 and 7.6 averaging at 5.5, and show a variation with depth (Alibo and Nozaki, 1999; Abbott et al., 2015). From our dataset, Griquatown carbonate $(Yb/Pr)_{SN}$ values are slightly closer to modern seawater than the Kuruman ones.

Carbonate-fraction and LA-ICP-MS carbonate data show very similar LREE/HREE slopes across a range of ΣREE (Figs. 3 and 6). It is not clear why LA-ICP-MS ΣREE show such a large range, but this could in part be due to the problem of correctly determining the concentration of the internal standard element for ablation yield corrections in heterogeneous carbonate mineral assemblages. These similarities help to validate the methodology, but also indicate that both individual carbonate mineral data and bulk carbonate values track the same geochemical processes. We interpret this to reflect primary seawater LREE/HREE variability, as supported by similarities between present-day microbialitic carbonates and seawater REE without strong fractionations (Webb and Kamber, 2000). If the carbonate were influenced, or even produced solely

by diagenesis, then it still appears to have quantitatively captured a consistent REY signal that is similar to modern seawater and significantly closer than the bulk rock values.

The Kuruman carbonate fraction data can be viewed in comparison with the conformably underlying Gamohaan carbonates of the Campbellrand Subgroup (Fig. 9). The steep Kuruman trend ($(Yb/Pr)_{SN} = 8.0$) contrasts with much shallower slope ($(Yb/Pr)_{SN} = 1.5$) in the microdrilled Gamohaan microbialites (Kamber and Webb, 2001). Bulk-rock microbialite samples from the slightly older Upper Nauga Formation within the Campbellrand Subgroup show similar shallow slopes, although more REE enriched (Voegelin et al., 2010). Other carbonate samples from the Campbellrand platform follow relatively flat trends (Eroglu et al., 2017). Incomplete REY patterns of the Gamohaan Formation published previously by Klein and Beukes (1989) show a flat or even HREE depleted trend. However, their bulk-rock analyses show relative high abundances of Al_2O_3 and SiO_2, indicating that the samples contained an additional component beyond pure carbonate. We use only carbonate data (Kamber and Webb 2001; Voegelin et al., 2010; Eroglu et al., 2017) that is free of allochtonous influences for further comparison with the overlying Asbestos Hills IFs.

The distinct carbonate patterns between the three stratigraphically-continuous formations, Gamohaan, Kuruman and Griquatown most likely reflect primary water column processes at varying water depths. The oldest Gamohaan Formation is subtidal (Sumner, 1997) and shows the flattest REY pattern (Kamber and Webb, 2001; Gallagher et al., 2017; Fig. 7). The transition from a stromatolite platform to siderite-rich and then oxide-rich IF is consistent with continued deepening of the basin (Klein and Beukes, 1989; Sumner, 1997). The Kuruman samples in this study were taken mainly from the oxide-rich section, indicating the greatest water depths and they display the steepest REY patterns (Fig. 7). The transition to the granular Griquatown Formation indicates a shallowing towards storm-wave base (Beukes and Klein, 1990) and their respective REY patterns are intermediate in slope. Present day seawater shows similar variations in seawater REE_{SN} patterns with $(Yb/Pr)_{SN}$ and La anomalies controlled by particle adsorption and desorption effects that change with depth (e.g. Piepgras and Jacobsen, 1992; Alibo and Nozaki, 1999; Abbott et al., 2015). The lack of correspondence for $(Yb/Pr)_{SN}$ and Y/Ho (Fig. 7) supports the assertion above that the carbonate fraction data are free of allochtonous interferences (Kamber and Webb, 2001). We discuss the changes in these parameters further below within the context of an evolutionary model.

An alternative explanation for differences between the formations could be LREE/HREE changes over time in seawater due to reservoir effects controlled by preferential HREE incorporation during massive deposition of $FeCO_3$ (e.g. Bau, 1993). However, the basin would need to be completely refreshed in REY to accommodate the jump from the Campbellrand to the Kuruman samples. Sustained Rayleigh fractionation over the Asbestos Hills subgroup is difficult to estimate due to poor constraints on depositional rates. A conceptual model of >2.4 Ga ocean redox structure based on REE in IF and carbonates (Planavsky et al., 2010) indicates a similar water column depth-gradient in REE and we consider this the most straightforward explanation.

5.3. Oxide fraction

The oxide fraction REE data show abundances below bulk rock values with a relative enrichment in the MREE (especially from Eu to Er, Fig. 10). We quantify the MREE enrichment (MREE/MREE*) here by calculating the deviation of shale-normalized Tb from the line of inferred linear slope from Pr to Yb. These REE were chosen since they lack anomalous behavior in their chemistry and Tb lies centrally between Pr and Yb in the lanthanide series. Since Tb lies 6 atomic numbers from Pr, including Pm and 5 from Yb excluding Y, MREE/MREE* was calculated as $Tb/((^5/_{11})Pr$

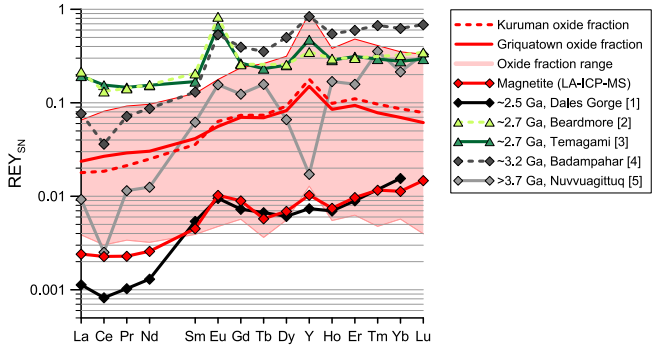

Fig. 10. REY_{SN} patterns of oxide fractions and magnetite in BIF. The red band shows the entire range of the oxide-fraction REY data from this study, with the averages of the Kuruman (dotted line) and Griquatown (continuous line) IF samples also shown. The different techniques used to determine the magnetite REY patterns are indicated as diamonds (LA-ICP-MS) and triangles (mineral separation/microdilling). The red line with diamond symbols are the results of this study. [1] Average of 11 magnetite samples of the Hamersley BIF (Alibert, 2016). [2] Average of 2 mineral separates of the Beardmore-Geraldton BIFs (CD-2 and VL-1, Barrett et al., 1988). [3] Average of 12 microdrilled magnetite bands of the Temagami IF (Bau and Alexander, 2009). [4] Average of 10 LA-ICP-MS analysed magnetites from the Badampahar Greenstone belt hosted IFs (Ghosh and Baidya, 2017). [5] Average of the silicate- poor and magnetite-rich BIFs in the Nuvvuagittuq Supracrustal Belt (Mloszewska et al., 2012). (For interpretation of the references to colour in this figure legend, the reader is referred to the web version of this article.)

$+(^{6}/_{11})$Yb). This gives a range of MREE/MREE* for the oxide fraction of 0.78–2.50 with an average of 1.49, indicating that the oxide fraction data have REE patterns that are predominantly convex upwards.

Enrichments in MREE have been shown before and often have a close relationship with the abundance of Fe, as seen for oxide-coatings on fossil foraminifera (Palmer and Elderfield, 1986), hydrothermal vent particulates (Sherrell et al., 1999), riverine Fe-rich organic colloids (Sholkovitz, 1995) and in Fe-rich anoxic porefluids (Haley et al., 2004). In the latter study, the enrichment was explained by dissolution of a surficial solid Fe-phase that inherited REE from seawater (Haley et al., 2004). An explanation for the oxide fraction Eu-Er enrichment might thus be related to preferential MREE adsorption onto ferric-iron particles during settling through the water column or during diagenetic mineral growth (Sherrell et al., 1999). Several jaspilitic IF samples (hematite/magnetite + quartz) from the Mozaan Formation also show MREE enrichments (Alexander et al., 2008; Bolhar et al., 2015). The very shallow depositional environment and a MREE enrichment seen in the riverine colloidal fraction (Sholkovitz, 1995; Bolhar & Van Kranendonk, 2007) suggest that these particles could exert a strong influence on REY distributions in the Mozaan IFs (Alexander et al., 2008). However, a MREE-enriched pattern has not been described in any detail for bulk-carbonate containing IF samples. This is most likely due to the difficulty in obtaining accurate and precise data due to the low abundance of REE in magnetite (Fig. 3), especially compared to other mineralogical fractions (Fig. 4).

Two different techniques have been used to determine magnetite-specific REE patterns in IF samples; LA-ICP-MS (Mloszewska et al., 2012; Alibert, 2016; Ghosh and Baidya, 2017) and microdrilling or mineral separation (Barrett et al., 1988; Bau and Alexander, 2009). Data produced by mineral separation or drilling have relatively high total REE concentration with a shallow LREE/HREE slope (Fig. 10). Some of these samples show high Al (0.4–1.2 wt%) and Zr (6–17 ppm, Bau and Alexander, 2009), suggesting the elevated values and relatively flat REE might be influenced by contamination from silicates. However, this method has not yet been validated against sequential extraction data for the same samples. Individual mineral data were produced for magnetite by LA-ICP-MS for the ca. 2.5 Ga Dales Gorge BIF in Australia (Alibert, 2016), the ca 3.1-3-3 Ga Badampahar Greenstone belt hosted BIF (Ghosh and Baidya, 2017) and the $\geq$3.75 Ga metamorphosed Nuvvuagittuq IFs (Mloszewska et al., 2012). The REE patterns of the latter study are not comparable to the unmetamorphosed IFs of the Transvaal Basin. Although the Badampahar BIF only consists of quartz and magnetite with minor Fe-silicates, is metamorphosed to lower amphibolite facies, and perhaps affected by alteration leading to negative Ce anomalies, the average magnetite REY pattern resembles our data (Fig. 10; Ghosh and Baidya, 2017). The magnetite data for the Dales Gorge (Alibert, 2016) are also closely comparable to the Kuruman/Griquatown IFs (Fig. 10), except for the LREE concentrations that are lower in the Dales Gorge samples. The low LREE values in the Dales Gorge magnetite result in a strong MREE enrichment. As the Transvaal magnetites have higher LREE values, the MREE enrichment here is less evident.

The oxide fraction data are much more enriched in REE compared to the LA-ICP-MS magnetite results. This could be due to sampling bias since only the larger magnetite aggregates were measured by laser ablation, which has insufficient spatial resolution to measure the predominant oxide-crystal size fraction that is below tens of μm in diameter. The larger magnetites could have been related to a different formation pathway to the more fine-grained fraction, perhaps with variable precursor minerals and/or pore-fluids during diagenesis. In comparison the sequential fraction data covers the entire oxide mineral budget and reflects an integrated history of all processes controlling REE partitioning.

Another possibility to explain the differences in oxalate extracted oxide and magnetite grains is the presence of phosphates that would also be digested in the oxalate step of the sequential extraction (Uusitalo and Tuhkanen, 2000). Very small grains or inclusions of REE-rich phosphate minerals such as xenotime, monazite and apatite, which have been described in the Dales Gorge IF (e.g. Li et al., 2011, Alibert, 2016), could potentially have a major influence on bulk-rock or even mineral-specific REY-data (Smith et al., 2008). In IFs these phosphate minerals can have varying patterns from extremely LREE enriched (monazite) to extremely LREE depleted (xenotime) (Alibert, 2016). The focus of the study by Alibert (2016) was on apatite with REE patterns that varied from near flat to LREE depleted. Although the phosphates are a significant REE host, they are only a minor constituent in the Dales Gorge IFs ($P_2O_5 \approx 0.2$ wt%). Based on similar patterns between the whole-rock and the apatite REEs and high REE concentrations in apatite, Alibert (2016) concluded that the iron oxides and carbonates carry only a small fraction of the whole-rock REE budget. Indeed, the apatites in the Hamersley basin are enriched in REY by ca. 1.5 orders compared to the carbonate LA-ICP-MS data in the Asbestos Hills (Fig. 11). However, in the Kuruman and Griquatown samples studied here, the average bulk rock P_2O_5 content is only 0.06 wt%. This is confirmed by the vast majority of previously-measured bulk-rock Asbestos Hills data with $P_2O_5 \leq 0.10$ wt% (Klein and Beukes, 1989; Beukes and Klein, 1990; Horstmann and Hälbich, 1995). Some magnetite-chert samples from the Kuruman IF are an exception to this and show slightly higher P_2O_5 with an average of 0.24 wt% (Horstmann and Hälbich, 1995). Apatite has not yet been identified in petrographic studies of the Asbestos Hills IFs.

Apatite nanoparticles, such as those found intergrown in magnetite of the Dales Gorge Member, Brockman IF (Li et al., 2011) could explain the minor quantities of P present in the Asbestos Hills IFs. Phosphorus was generally below detection limit for all of the sequential extraction steps, partly due to the relatively poor detection limit for P by ICP-OES and ICP-MS. However, there is a correlation between bulk-rock P_2O_5 determined by XRF and the $(Yb/Pr)_{SN}$ ratio in the oxalate extracted fraction (Fig. 12). This weak correlation is independent of the oxide to carbonate ratio (as given by the fraction normalization values).

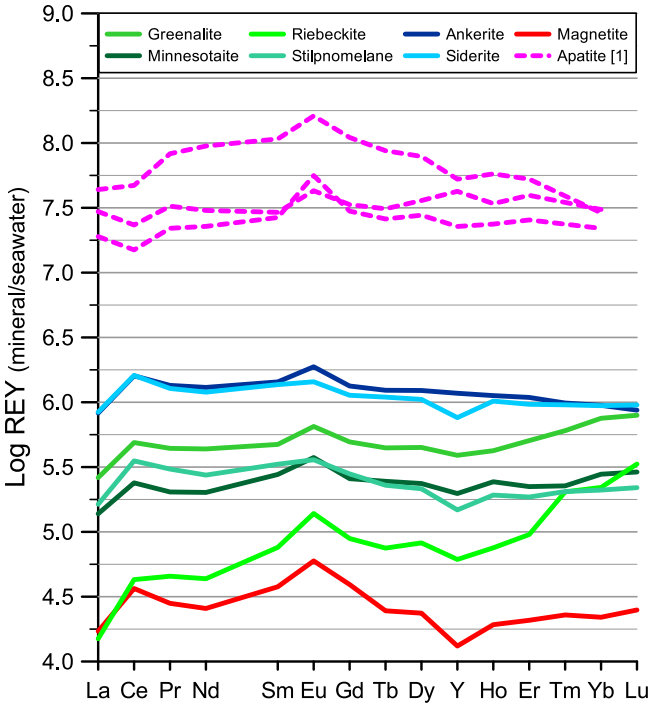

Fig. 11. Average REY mineral composition normalized to North Pacific Deep Water (NPDW) seawater at 2500 m depth (Alibo and Nozaki, 1999). The contemporaneous seawater Ce anomaly was removed in the ratio calculation by interpolating between Pr and Nd and effectively normalizing to Ce*. The flatter the lines, the more they resemble present day seawater. The apatites from the Hamersley IFs ([1], Alibert, 2016) included here are ca. 1.5 orders more enriched in REY than the carbonates from the Asbestos Hills.

The P-rich samples coincide with steeper REE slopes, and could potentially be related to the presence of LREE depleted, HREE enriched phosphate minerals such as apatite or xenotime (Alibert, 2016). Nanoparticulate apatite would be digested during the oxalate-step (Uusitalo and Tuhkanen, 2000). However, there seems to be no relationship between bulk-rock P_2O_5 and MREE enrichment (Fig. 12).

In summary, the oxide fraction displays a distinctive REY slope, but since much of the magnetite most likely crystallized during diagenesis (Klein, 2005), the oxide fraction data cannot be used to directly infer seawater REE variability. Very low ΣREE in precursor oxide minerals would mean that any LREE or HREE released during diagenetic magnetite formation would have had a minor effect on the other fractions.

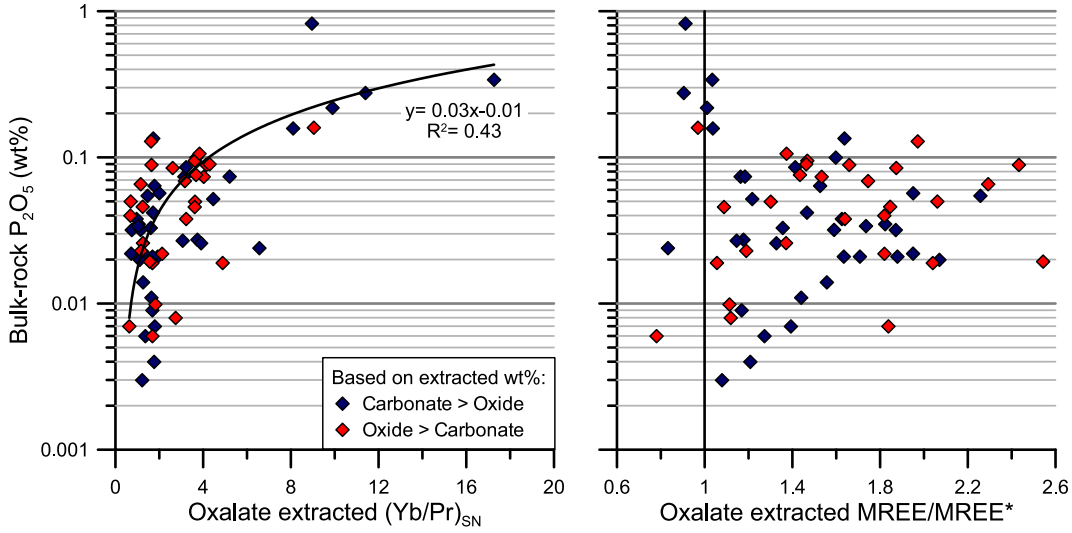

Fig. 12. Bulk-rock P_2O_5 versus the oxalate extracted $(Yb/Pr)_{SN}$ and MREE/MREE*. The red diamonds are samples with more wt% oxide-present than the carbonates, the blue samples are more carbonate rich than oxide. See text for discussion. (For interpretation of the references to colour in this figure legend, the reader is referred to the web version of this article.)

5.4. Silicate-bound REE

The wide range in overall REE abundances for the silicate fraction (Fig. 6c) is due to dilution by chert (Fig. 13a). We show this by plotting the fraction-normalized Si content (bulk-rock minus acetate and oxalate extracted Si, since Si cannot be measured directly) against fraction-normalized ΣREE (Fig. 13a). Samples with low ΣREE are close to pure SiO_2 (equivalent to 46.7 wt% Si), and higher REE concentrations thus reflect the increasing abundance of other silicate minerals. Our data indicate that near-pure cherts have up to three orders of magnitude lower REE abundance than Fe-silicate rich samples. Care should thus be taken when selecting (close to) pure chert samples for REE analysis to ensure their purity. The abundance of REE is closely correlated to Zr (Fig. 13b), especially when Zr > 1 ppm, indicating that the REEs in this fraction are, at least partially, controlled by detrital input.

Considerable variation is seen in our silicate fraction ΣREE and LREE/HREE data that was not observed as extensively in the carbonate and oxide fractions (Fig. 6). The average LA-ICP-MS data of all the measured silicate minerals have a positive REE_{SN} slope (Fig. 3), and thus a rock made from a mixture of these minerals should retain $(Yb/Pr)_{SN} > 1$. However, many of the sequential extraction results for the silicate fraction show $(Yb/Pr)_{SN} < 1$. We plot fraction-normalized Mg, Al and bulk-rock Na in Fig. 13c–e, to investigate mineralogical control on $(Yb/Pr)_{SN}$. High Mg concentrations should indicate the presence of minnesoitate or greenalite, whereas Al is mainly bound in stilpnomelane. Sodium can be used to track the presence of riebeckite. Since Na-acetate was used to dissolve the carbonate fraction, bulk-rock Na values were normalized to the silicate fraction in order to estimate riebeckite abundance. This implicitly assumes that all bulk-rock Na was bound to riebeckite. Riebeckite is generally considered to be of secondary origin related to external Na input (e.g. Trendall and Blockey, 1970; Beukes and Dreyer, 1986), possibly confirmed by the absence of a distinct La anomaly (Fig. 3).

The Al-rich lutite samples show $(Yb/Pr)_{SN} \approx 1$ indicating relatively unfractionated LREE/HREE. The most REE enriched stilpnomelanes (Fig. 3) show the flattest patterns of all individual silicate minerals that were measured. The grain size of silicates in the lutites are too small to

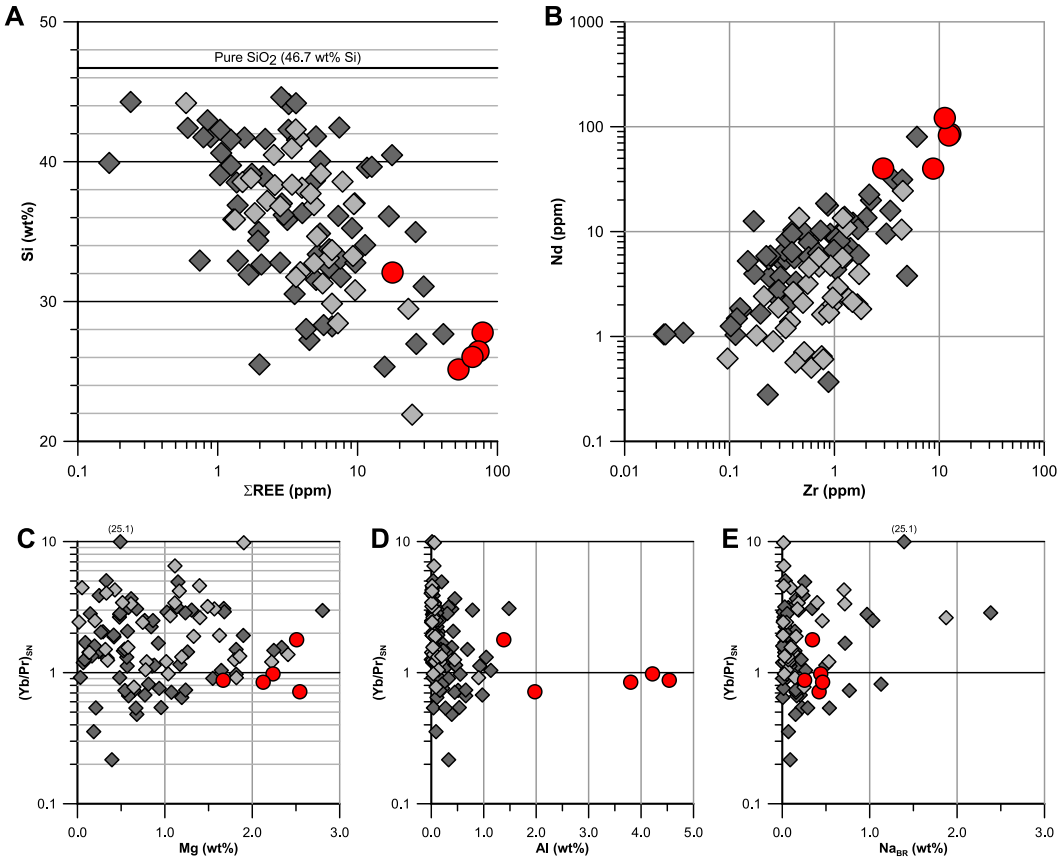

Fig. 13. Silicate fraction-normalized plots for the Asbestos Hills IFs. The red dots are the five lutite samples and the diamonds are the IF samples from the Griquatown (dark) and the Kuruman Formations (light). (A) ΣREE (ppm) versus calculated Si (wt%), where Si was determined by subtracting the previous extractions from the bulk-rock data. (B) Zr (ppm) versus Nd (ppm). (C–E) Mg, Al and Na versus $(Yb/Pr)_{SN}$ respectively. The bulk-rock Na data were normalized against the silicate fraction, assuming all Na was extracted during the HF leach. See text for discussion. (For interpretation of the references to colour in this figure legend, the reader is referred to the web version of this article.)

measure directly by LA-ICP-MS, but a high Al content, in combination with high REE and unfractionated LREE/HREE, suggests stilpnomelane control. Magnesium-rich samples are more difficult to interpret and Mg shows no clear control on $(Yb/Pr)_{SN}$. The Na-rich samples tend to have a $(Yb/Pr)_{SN}$ ratio > 1, but a clear correlation is lacking. No correlations were found between silicate fraction $(Yb/Pr)_{SN}$ and bulk-rock P, S or fraction-normalized Si. The complex REE patterns in the silicate fraction cannot be readily related to single processes or mineralogy. Variations on a sample scale that control REE sources, mineralogy and potential formation processes are more likely to be responsible for heterogeneity in the samples.

5.5. Depositional environments based on REY

Fraction-specific REY data enable a reassessment of seawater chemical evolution from the Campbellrand into the Asbestos Hills Subgroups, immediately prior to the GOE. Our new fraction and mineral data lack negative Ce anomalies. This indicates that the oxidation state of the basin was too low to preserve Mn-oxyhydroxides (e.g. Bau and Dulski, 1996). Although there might have been some Mn-cycling mediated by biological processes (Johnson et al., 2013), the oxidation state of the basin and the presence of ferrous Fe prevented the preservation of Mn-oxyhydroxides and thus negative Ce anomalies.

In our conceptual model for the evolution from Gamohaan to Griquatown times (Fig. 14), REE could have been incorporated into Kuruman and Griquatown IF through an Fe-(hydro)oxide pathway. In this model, ferrous Fe was oxidized to insoluble ferric iron in the photic zone, either directly by oxygen produced by photosynthesis (e.g. Godfrey and Falkowski, 2009) or via ferroautotrophy (e.g. Konhauser et al., 2002). We assume in this pathway that seawater REEs were quantitatively sorbed onto ferric (oxy)hydroxide, or other ferric precursor, due to the relatively high and uniform partition coefficients (K_d) for Fe-(hydr)oxides (Quinn et al., 2006) and high Fe/REE ratios in the system. This is supported by the fact that the bulk rock REY patterns resemble seawater. Once precipitated, ferric oxyhydroxides could have been reduced and would have released Fe^{2+}, P and REEs into porewater and/or minerals that were forming contemporaneously during diagenesis. Recent models have argued for a strong control by dissimilatory iron reduction (DIR) in which organic matter could have reduced ferric Fe and combined that with HCO_3^- to form ferrous Fe-carbonates (e.g. Johnson et al., 2008; Heimann et al., 2010). REEs could have been largely sequestered into carbonate, but also minerals such as iron oxides, silicates and apatite. Any unconsumed Fe-(oxy)hydroxides could, through reaction with the ferrous Fe-sources mentioned above, have produced magnetite and/or its precursors.

Alibert (2016) studied REY partitioning between different minerals in BIF from the Hamersley basin, and linked it to a similar Fe-(hydro)oxide pathway and DIR model. Apatite was shown in this study to inherit seawater-like REE from a silica-ferric oxyhydroxide co-precipitate, whilst hematite, greenalite, siderite or ankerite, showed REE typical of equilibration with pore-water. Greenalite REE distribution resembled experimental distribution patterns between clays and saline solutions, and could have reflected direct precipitation from pore-water enriched in silica, Fe^{2+} and REEs (Alibert, 2016). If we apply a similar rationale to the Asbestos Hills mineral-specific REE data, then carbonate shows the closest similarity to modern seawater REE, with only minor differences in the La, Eu and Y anomalies. We were unable to test this against apatite partitioning, due to low P_2O_5 abundances and a lack of apatite in our study. The carbonates we measured are arguably even less fractionated from modern seawater than the Hamersley apatites used in Alibert (2016) (Fig. 11), and due to their higher abundance and ease of measurement, a potentially

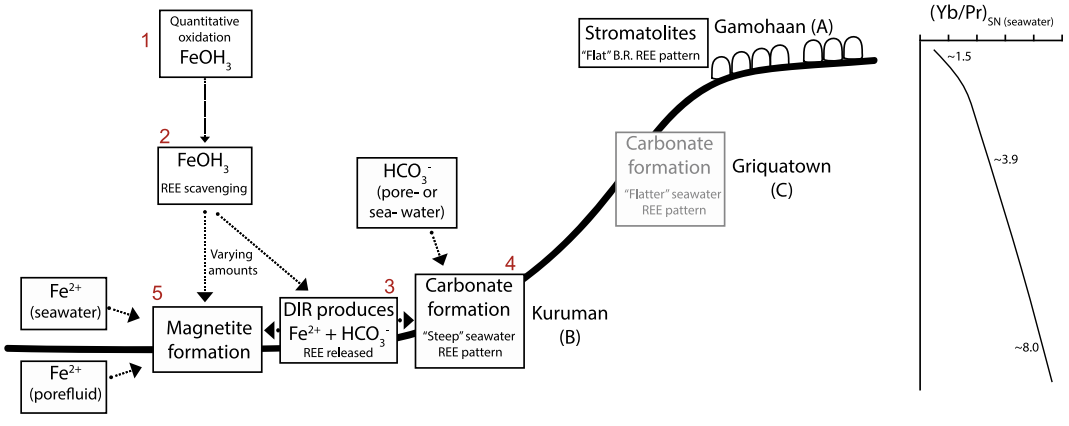

#: Process:	REE behavior:
1: Quantitative Fe^{2+} oxidation in photic zone	-
2: REE scavenging onto the ferrihydrite	Seawater REE pattern
3: Part of $FeOH_3$ reduced via DIR at seafloor, producing ferric Fe and HCO_3^-	REEs released and cycled back
4: Product Fe^{2+} and HCO_3^- form Fe-carbonates, with additional HCO_3^- input	Depth dependent seawater pattern
5: Remaining $FeOH_3$ forms magnetite precursor with porefluid, DIR or seawater Fe^{2+}	Mixed REE pattern

Fig. 14. Conceptual depositional environments and REE behaviour from Gamohaan (A), through Kuruman (B), to Griquatown (C) times. Average $(Yb/Pr)_{SN}$ data for Gamohaan formation from Kamber and Webb (2001).

more suitable tracer of ancient seawater chemistry. In addition to this, some Fe silicate microgranules, found along sedimentary laminations, also closely resemble seawater $(Yb/Pr)_{SN}$ (Fig. 11). A primary formation pathway for Fe-silicates has been previously suggested (Rasmussen et al., 2013, 2015, 2017) and our stilpnomelane and minnesotaite data show similar REE distributions to the carbonate fraction (Fig. 11). Magnetite in contrast shows strongly deviating REE from seawater signatures, possibly reflecting preferential adsorption of MREE during diagenetic growth as suggested above (Section 5.3). Riebeckite is also strongly fractionated, consistent with a probable later stage of secondary growth (e.g. Trendall and Blockey, 1970).

Primary water-column precipitation of iron carbonates presents a plausible and attractive explanation for the close similarity in REY behaviour between the carbonate fraction of IF and Fe-poor carbonate rocks of the upper Campbellrand Subgroup (Gamohaan Fm). Although classic interpretations for the C and Fe isotope composition of IF carbonates require formation exclusively below the sediment–water interface *via* organic carbon remineralisation and dissimilatory Fe(III) reduction (e.g. Heimann et al., 2010), it is conceivable that similar processes may have also occurred, at least partially, in the overlying water column (c.f. von Blanckenburg et al., 2008 for microbial carbonate). Such interpretation, however, remains speculative and requires further investigation.

Regardless of the formation pathway for the carbonate, it appears to have closely captured a primary seawater REY signature. Data from the Asbestos Hills subgroup reveals a REE-stratified basin with increasing $(Yb/Pr)_{SN}$, increasing La anomaly and relatively constant Y/Ho related to increasing water depth. This interpretation is consistent into the Campbellrand Subgroup for $(Yb/Pr)_{SN}$, whilst the other anomalies and ratios are more variable (Fig. 7). A relative time sequence of events can be envisaged as follows. A shallow water stromatolitic platform was deposited in the Campbellrand and was drowned by an Fe-rich basin as the relatively deepwater Kuruman IF was deposited conformably on top. The transition and subsequent shallowing of the basin from the oxide-rich Kuruman to the carbonate-rich Griquatown Formation was captured by lithological changes (Beukes, 1984; Beukes and Klein 1990) and chemostratigraphy (Oonk et al., 2017) that tracks the shift in carbonate $(Yb/Pr)_{SN}$ ratios observed here. REY data for the Griquatown formation are very similar to the modern surface ocean with $(Yb/Pr)_{SN}$ of ca. 5.5 (Alibo and Nozaki, 1999; Abbott et al., 2015) consistent with the dominance of aeolian REE inputs. This suggests that similar processes controlled REY distribution in the shallow Paleoproterozoic oceans to those seen today. However, data from the deeper water Kuruman formation record much more fractionated HREE/LREE, with $(Yb/Pr)_{SN}$ up to 16, much higher than the maximum $(Yb/Pr)_{SN}$ of 8 observed in modern seawater (Piepgras and Jacobsen, 1992; German et al., 1995; Byrne and Sholkovitz, 1996; Alibo and Nozaki, 1999; Abbott et al., 2015).

The abundance of REY in seawater is controlled by weathering and hydrothermal inputs, particle adsorption effects, ocean circulation and regeneration from sinking particles or seafloor sediments (Elderfield et al., 1988; Byrne and Kim, 1990). Hydrothermal, aeolian and riverine inputs cannot alone produce the elevated Kuruman $(Yb/Pr)_{SN}$ values, indicating control by exit pathways. Adsorption of REE is influenced most strongly by the presence of organic coatings on mineral surfaces that strongly draw down the LREE (Byrne and Kim, 1990). Little is known about the distribution of dissolved organic carbon in the Asbestos Hills basin, but total organic carbon in both the Griquatown and Kuruman IF is consistently at or below detection limits and thus not reported here. The deeper water Kuruman IF is much richer in magnetite and poorer in carbonate than the Griquatown (section 4.3.2) that could be explained by a decreased role of DIR with depth. Partial DIR would allow a significant portion of the ferric iron to form magnetite, whereas near complete DIR at shallower water depths resulted in carbonate domination. Near complete oxidation of Fe in surface waters could have led to very low Fe^{2+} concentrations, which explains the lack of Fe-carbonates in the Campbellrand Formation. In this scenario, organic carbon is most likely to have been the limiting reactant during DIR and (near) completely consumed in both shallow and deeper waters. Variable abundance of organic coatings is thus impossible to assess in controlling REE distribution during sequestration of REY into BIF. However, if more organic matter was available at the time of deposition of the Griquatown formation it should have depleted LREE more strongly than observed in our data.

Rare earth elements reach progressively higher $(Yb/Pr)_{SN}$ with depth in the upper 1–2 km of the modern oceans due to progressive adsorption onto sinking particles in the water column. In contrast, La anomalies are most positive in surface waters (Alibo and Nozaki, 1999) and reach more positive values than observed in our Asbestos Hills data (reflected in systematically low La values in mineral data plotted in Fig. 11). With increasing depth, $(Yb/Pr)_{SN}$ falls due to regeneration of REE from sinking particles or due to release of a diagenetic component from seafloor sediments. Ocean circulation may also play a role by recycling REE-rich and less $(Yb/Pr)_{SN}$ fractionated water to the ocean floor. All of these processes could have played a role in the ferruginous Paleoproterozoic ocean leading to a reduction in regeneration and recycling that enabled $(Yb/Pr)_{SN}$ to reach the most positive values observed in the Kuruman Formation.

6. CONCLUSIONS

A three-step sequential extraction procedure was developed for rare earth element analysis in iron formations in order to more accurately identify primary seawater signatures than has been previously possible through bulk rock analysis. The results for carbonate, oxide and silicate-dominated fractions were successfully validated through mass balance against bulk rock data and by comparison against mineral REY data determined in individual grains

by LA-ICP-MS. Our new method was applied to the ca. 3.4 Ga Kuruman and Griquatown Formations of the Transvaal Supergroup, South Africa. Key findings can be summarized as follows:

- Although bulk rock REY data show on first approximation a close correlation to expected seawater variability, they were influenced to a small but significant degree by allochtonous material, even in rocks with relatively low Al_2O_3 and Zr concentrations. Bulk rock data should thus be used with caution to reconstruct primary environmental trace element variations in most IF samples.
- Sequential extraction of carbonate avoids contamination from detrital components and thus tracks more closely primary seawater variability in IF. Carbonate extracted from Paleoproterozoic BIF overlaps, but extends beyond the range in REY variability seen in the modern oceans.
- The oxide fraction was found to be the most REY-depleted and is thus susceptible to allochthonous influences. This magnetite-dominated fraction was consistently more enriched in MREE and lacks the positive La anomaly seen in other fractions.
- The silicate fraction was most strongly influenced by allochthonous sources and a highly variable silicate-mineralogy. Some individual grains of silicate minerals including minnesotaite and stilpnomelane show REY signatures similar to carbonate and hence seawater.

Sequential fraction data from the Asbestos Hills subgroup samples together with previously published carbonate data from the underlying Gamohaan Formation was used to build a conceptual deposition model in the Griqualand West Basin. The basin was found to show Yb/Pr and La anomaly stratification with constant seawater-like Y/Ho ratios. The absence of Ce anomalies indicate that conditions were reducing with respect to Ce and by extension to Mn. A shift from oxide- to carbonate-dominated IF from Kuruman to Griquatown formations is interpreted to reflect an increase in DIR activity from the deeper to shallower parts of the basin.

ACKNOWLEDGEMENTS

We thank Balz Kamber, Robert Bolhar aan an anonymous reviewer for comments that helped to improve the manuscript. Funding and support was provided by ASSMANG Ltd. for the research unit PRIMOR at Rhodes University. We thank Mr. T. Rabuda and EP Ferreira from SOUTH32 in Hotazel for providing access to the drillcores used in this study. Laboratory work was supported by the Netherlands Research Centre for Integrated Solid Earth Sciences (grant number 2.2.3). PM acknowledges financial support from Rhodes University through the Hugh Kelly fellowship. Helen de Waard and Ton Zalm are thanked for assistance in the lab.

REFERENCES

Abbott A. N., Haley B. A., McManus J. and Reimers C. E. (2015) The sedimentary flux of dissolved rare earth elements to the ocean. *Geochim. Cosmochim. Acta* **154**, 186–200.

Alexander B. W., Bau M., Andersson P. and Dulski P. (2008) Continentally-derived solutes in shallow Archean seawater: rare earth element and Nd isotope evidence in iron formation from the 2.9 Ga Pongola Supergroup, South Africa. *Geochim. Cosmochim. Acta* **72**, 378–394.

Alibert C. (2016) Rare earth elements in Hamersley BIF minerals. *Geochim. Cosmochim. Acta* **184**, 311–328.

Alibo D. S. and Nozaki Y. (1999) Rare earth elements in seawater: particle association, shale-normalization, and Ce oxidation. *Geochim. Cosmochim. Acta* **63**, 363–372.

Babechuk M. G., Widdowson M., Murphy M. and Kamber B. S. (2015) A combined Y/Ho, high field strength element (HFSE) and Nd isotope perspective on basalt weathering, Deccan Traps, India. *Chem. Geol.* **396**, 25–41.

Baldwin G. J., Thurston P. C. and Kamber B. S. (2011) High-precision rare earth element, nickel, and chromium chemistry of chert microbands pre-screened with in-situ analysis. *Chem. Geol.* **285**, 133–143.

Barley M. E., Pickard A. L. and Sylvester P. J. (1997) Emplacement of a large igneous province as a possible cause of banded iron formation 2.45 billion years ago. *Nature* **385**, 55–58.

Barrett T., Fralick P. and Jarvis I. (1988) Rare-earth-element geochemistry of some Archean iron formations north of Lake Superior, Ontario. *Can. J. Earth Sci.* **25**, 570–580.

Bau M. (1993) Effects of syn-and post-depositional processes on the rare-earth element distribution in Precambrian iron-formations. *Eur. J. Mineral.* **5**, 257–267.

Bau M. (1996) Controls on the fractionation of isovalent trace elements in magmatic and aqueous systems: evidence from Y/Ho, Zr/Hf, and lanthanide tetrad effect. *Contrib. Mineral. Petrol.* **123**, 323–333.

Bau M. and Alexander B. (2006) Preservation of primary REE patterns without Ce anomaly during dolomitization of Mid-Paleoproterozoic limestone and the potential re-establishment of marine anoxia immediately after the "Great Oxidation Event". *South African J. Geol.* **109**, 81–86.

Bau M. and Alexander B. W. (2009) Distribution of high field strength elements (Y, Zr, REE, Hf, Ta, Th, U) in adjacent magnetite and chert bands and in reference standards FeR-3 and FeR-4 from the Temagami iron-formation, Canada, and the redox level of the Neoarchean ocean. *Precambrian Res.* **174**, 337–346.

Bau M. and Dulski P. (1996) Distribution of yttrium and rare-earth elements in the Penge and Kuruman iron-formations, Transvaal Supergroup, South Africa. *Precambrian Res.* **79**, 37–55.

Bau M. and Koschinsky A. (2009) Oxidative scavenging of cerium on hydrous Fe oxide: Evidence from the distribution of rare earth elements and yttrium between Fe oxides and Mn oxides in hydrogenetic ferromanganese crusts. *Geochem. J.* **43**, 37–47.

Bau M. and Möller P. (1993) Rare earth element systematics of the chemically precipitated component in Early Precambrian iron formations and the evolution of the terrestrial atmosphere-hydrosphere-lithosphere system. *Geochim. Cosmochim. Acta* **57**, 2239–2249.

Bekker A., Slack J. F., Planavsky N. J., Krapež B., Hofmann A., Konhauser K. O. and Rouxel O. J. (2010) Iron formation: the sedimentary product of a complex interplay among mantle, tectonic, oceanic, and biospheric processes. *Economic Geol.* **105**, 467–508.

Beukes N. J. (1984) Sedimentology of the Kuruman and Griquatown iron-formations, Transvaal supergroup, Griqualand West, South Africa. *Precambrian Res.* **24**, 47–84.

Beukes N. J. and Dreyer C. J. B. (1986) Crocidolite deposits of the Pomfret area, Griqualand West. 911–922. In *Mineral Deposits of Southern Africa* (eds. C. R. Anhaeusser and S. Maske). Geol. Soc. S. Afr, Johannesburg, p. 2335.

Beukes N. J. and Gutzmer J. (2008) Origin and paleoenvironmental significance of major iron formations at the Archean-Paleoproterozoic boundary. *Rev. Econ. Geol.* **15**, 5–47.

Beukes N. J. and Klein C. (1990) Geochemistry and sedimentology of a facies transition—from microbanded to granular iron-formation—in the early Proterozoic Transvaal Supergroup, South Africa. *Precambrian Res.* **47**, 99–139.

Bolhar R., Kamber B. S., Moorbath S., Fedo C. M. and Whitehouse M. J. (2004) Characterisation of early Archaean chemical sediments by trace element signatures. *Earth Planet. Sci. Lett.* **222**, 43–60.

Bolhar R. and Van Kranendonk M. J. (2007) A non-marine depositional setting for the northern Fortescue Group, Pilbara Craton, inferred from trace element geochemistry of stromatolitic carbonates. *Precambrian Res.* **155**, 229–250.

Bolhar R., Hofmann A., Siahi M., Feng Y.-X. and Delvigne C. (2015) A trace element and Pb isotopic investigation into the provenance and deposition of stromatolitic carbonates, ironstones and associated shales of the ~3.0Ga Pongola Supergroup, Kaapvaal Craton. *Geochim. Cosmochim. Acta* **158**, 57–78.

Byrne R. H. and Kim K. H. (1990) Rare earth element scavenging in seawater. *Geochim. Cosmochim. Acta* **54**, 2645–2656.

Byrne R. H. and Sholkovitz E. R. (1996) Marine chemistry and geochemistry of the lanthanides. *Handbook on the Physics and Chemistry of Rare Earths* **23**, 497–593.

Canfield D. E. (2005) The early history of atmospheric oxygen: homage to Robert M. Garrels. *Annu. Rev. Earth Planet. Sci.* **33**, 1–36.

Delvigne C., Cardinal D., Hofmann A. and André L. (2012) Stratigraphic changes of Ge/Si, REE Y and silicon isotopes as insights into the deposition of a Mesoarchaean banded iron formation. *Earth Planet. Sci. Lett.* **355**, 109–118.

Derry L. A. and Jacobsen S. B. (1990) The chemical evolution of Precambrian seawater: evidence from REEs in banded iron formations. *Geochim. Cosmochim. Acta* **54**, 2965–2977.

Dymek R. F. and Klein C. (1988) Chemistry, petrology and origin of banded iron-formation lithologies from the 3800 MA isua supracrustal belt, West Greenland. *Precambrian Res.* **39**, 247–302.

Elderfield H., Hawkesworth C., Greaves M. and Calvert S. (1981) Rare earth element geochemistry of oceanic ferromanganese nodules and associated sediments. *Geochim. Cosmochim. Acta* **45**, 513–528.

Elderfield H., Whitfield M., Burton J. D., Bacon M. P. and Liss P. S. (1988) The oceanic chemistry of the rare-earth elements. *Philos. Mag. A* **325**, 105–126.

Eroglu S., van Zuilen M. A., Taubald H., Drost K., Wille M., Swanner E. D., Beukes N. D. and Schoenberg R. (2017) Depth-dependent $\delta^{13}C$ trends in platform and slope settings of the Campbellrand-Malmani carbonate platform and possible implications for Early Earth oxygenation. *Precambrian Res.* **302**, 122–139.

Frei R., Dahl P. S., Duke E. F., Frei K. M., Hansen T. R., Frandsson M. M. and Jensen L. A. (2008) Trace element and isotopic characterization of Neoarchean and Paleoproterozoic iron formations in the Black Hills (South Dakota, USA): assessment of chemical change during 2.9–1.9 Ga deposition bracketing the 2.4–2.2 Ga first rise of atmospheric oxygen. *Precambrian Res.* **162**, 441–474.

Gallagher M., Whitehouse M. J. and Kamber B. S. (2017) The Neoarchaean surficial sulphur cycle: An alternative hypothesis based on analogies with 20th-century atmospheric lead. *Geobiology* **15**, 385–400.

German C. R., Masuzawa T., Greaves M. J., Elderfield H. and Edmond J. M. (1995) Dissolved rare earth elements in the Southern Ocean: Cerium oxidation and the influence of hydrography. *Geochim. Cosmochim. Acta* **59**, 1551–1558.

Godfrey L. V. and Falkowski P. G. (2009) The cycling and redox state of nitrogen in the Archaean ocean. *Nat. Geosci.* **2**, 725–729.

Ghosh R. and Baidya T. K. (2017) Mesoarchean BIF and iron ores of the Badampahar greenstone belt, Iron Ore Group, East Indian Shield. *J. Asian Earth Sci.* **150**, 25–44.

Gumsley A. P., Chamberlain K. R., Bleeker W., Soderlund U., de Kock M. O., Larsson E. R. and Bekker A. (2017) Timing and tempo of the great oxidation event. *Proc. Natl. Acad. Sci. U. S. A.* **114**, 1811–1816.

Haley B. A., Klinkhammer G. P. and McManus J. (2004) Rare earth elements in pore waters of marine sediments. *Geochim. Cosmochim. Acta* **68**, 1265–1279.

Halverson G. P., Poitrasson F., Hoffman P. F., Nédélec A., Montel J. and Kirby J. (2011) Fe isotope and trace element geochemistry of the Neoproterozoic syn-glacial Rapitan iron formation. *Earth Planet. Sci. Lett.* **309**, 100–112.

Haynes, W. M. (2017) CRC Handbook of Chemistry and Physics CRC Press/Taylor and Francis, Boca Raton, FL, Internet Version (hbcponline.com).

Heimann A., Johnson C. M., Beard B. L., Valley J. W., Roden E. E., Spicuzza M. J. and Beukes N. J. (2010) Fe, C, and O isotope compositions of banded iron formation carbonates demonstrate a major role for dissimilatory iron reduction in~ 2.5 Ga marine environments. *Earth Planet. Sci. Lett.* **294**, 8–18.

Horstmann U. E. and Hälbich I. W. (1995) Chemical composition of banded iron-formations of the Griqualand West Sequence, Northern Cape Province, South Africa, in comparison with other Precambrian iron formations. *Precambrian Res.* **72**, 109–145.

Jarvis K. E., Gray A. L. and McCurdy E. (1989) Avoidance of spectral interference on europium in inductively coupled plasma mass spectrometry by sensitive measurement of the doubly charged ion. *J. Anal. At. Spectrom.* **4**, 743–747.

Jochum K. P., Nohl U., Herwig K., Lammel E., Stoll B. and Hofmann A. W. (2005) GeoReM: a new geochemical database for reference materials and isotopic standards. *Geostandards Geoanal. Res.* **29**, 333–338.

Johnson C. M., Beard B. L. and Roden E. E. (2008) The iron isotope fingerprints of redox and biogeochemical cycling in modern and ancient Earth. *Annu. Rev. Earth Planet. Sci.* **36**, 457–493.

Johnson J. E., Webb S. M., Thomas K., Ono S., Kirschvink J. L. and Fischer W. W. (2013) Manganese-oxidizing photosynthesis before the rise of cyanobacteria. *Proc. Natl. Acad. Sci. U. S. A.* **110**, 11238–11243.

Kamber B. S. and Webb G. E. (2001) The geochemistry of late Archaean microbial carbonate: implications for ocean chemistry and continental erosion history. *Geochim. Cosmochim. Acta* **65**, 2509–2525.

Kamber B. S., Greig A. and Collerson K. D. (2005) A new estimate for the composition of weathered young upper continental crust from alluvial sediments, Queensland, Australia. *Geochim. Cosmochim. Acta* **69**, 1041–1058.

Kampmann T. C., Gumsley A. P., de Kock M. O. and Söderlund U. (2015) U-Pb geochronology and paleomagnetism of the Westerberg Sill Suite, Kaapvaal Craton-Support for a coherent Kaapvaal-Pilbara Block (Vaalbara) into the Paleoproterozoic? *Precambrian Res.* **269**, 58–72.

Klein C. and Beukes N. J. (1989) Geochemistry and sedimentology of a facies transition from limestone to iron-formation deposition in the early Proterozoic Transvaal Supergroup, South Africa. *Econ. Geol.* **84**, 1733–1774.

Klein C. (2005) Some Precambrian banded iron-formations (BIFs) from around the world: Their age, geologic setting, mineralogy, metamorphism, geochemistry, and origins. *Am. Mineral.* **90**, 1473–1499.

Konhauser K. O., Hamade T., Raiswell R., Morris R. C., Ferris F. G., Southam G. and Canfield D. E. (2002) Could bacteria have formed the Precambrian banded iron formations? *Geology* **30**, 1079–1082.

Konhauser K. O., Planavsky N. J., Hardisty D. S., Robbins L. J., Warchola T. J., Haugaard R., Lalonde S. V., Partin C. A., Oonk P. B. H., Tsikos H., Lyons T. W., Bekker A. and Johnson C. M. (2017) Iron formations: a record of neoarchean to paleoproterozoic environmental history. *Earth Sci. Rev.* **172**, 140–177.

Land M., Öhlander B., Ingri J. and Thunberg J. (1999) Solid speciation and fractionation of rare earth elements in a spodosol profile from northern Sweden as revealed by sequential extraction. *Chem. Geol.* **160**, 121–138.

Lantink M. L., Oonk P. B. H., Floor G. H., Tsikos H. and Mason P. R. D. (2018) Fe isotopes of a 2.4 Ga hematite-rich IF constrain marine redox conditions around the GOE. *Precambrian Res.* **305**, 218–235.

Lawrence M. G., Greig A., Collerson K. D. and Kamber B. S. (2006) Rare earth element and yttrium variability in South East Queensland waterways. *Aquatic Geochem.* **12**, 39–72.

Lepland A., Arrhenius G. and Cornell D. (2002) Apatite in early Archean Isua supracrustal rocks, southern West Greenland: its origin, association with graphite and potential as a biomarker. *Precambrian Res.* **118**, 221–241.

Li Y., Konhauser K. O., Cole D. R. and Phelps T. J. (2011) Mineral ecophysiological data provide growing evidence for microbial activity in banded-iron formations. *Geology* **39**, 707–710.

McLennan S. M. (1989) Rare earth elements in sedimentary rocks; influence of provenance and sedimentary processes. *Rev. Mineral. Geochem.* **21**, 169–200.

Miyano T. and Beukes N. (1984) Phase relations of stilpnomelane, ferri-annite, and riebeckite in very low-grade metamorphosed iron-formations. *South African J. Geol.* **87**, 111–124.

Mloszewska A. M., Pecoits E., Cates N. L., Mojzsis S. J., O'Neil J., Robbins L. J. and Konhauser K. O. (2012) The composition of Earth's oldest iron formations: the Nuvvuagittuq Supracrustal Belt (Québec, Canada). *Earth Planet. Sci. Lett.* **317**, 331–342.

Moffett J. W. (1994) The relationship between cerium and manganese oxidation in the marine environment. *Limnol. Oceanogr.* **39**, 1309–1318.

Nakada R., Takahashi Y. and Tanimizu M. (2016) Cerium stable isotope ratios in ferromanganese deposits and their potential as a paleo-redox proxy. *Geochim. Cosmochim. Acta* **181**, 89–100.

Nel B. P. (2013) Petrography and geochemistry of iron formations of the Paleoproterozoic Koegas Subgroup, Transvaal Supergroup, Griqualand West, South Africa, MSc-thesis, University of Johannesburg, 134p.

Oonk P. B. H., Tsikos H., Mason P. R. D., Henkel S., Staubwasser M., Fryer L., Poulton S. W. and Williams H. M. (2017) Fraction-specific controls on the trace element distribution in BIF: Implications for trace metal stable isotope proxies. *Chem. Geol.* **474**, 17–32.

Palmer M. and Elderfield H. (1986) Rare earth elements and neodymium isotopes in ferromanganese oxide coatings of Cenozoic foraminifera from the Atlantic Ocean. *Geochim. Cosmochim. Acta* **50**, 409–417.

Pecoits E., Gingras M., Barley M., Kappler A., Posth N. and Konhauser K. (2009) Petrography and geochemistry of the Dales Gorge banded iron formation: Paragenetic sequence, source and implications for palaeo-ocean chemistry. *Precambrian Res.* **172**, 163–187.

Pickard A. (2003) SHRIMP U-Pb zircon ages for the Palaeoproterozoic Kuruman Iron Formation, Northern Cape Province, South Africa: evidence for simultaneous BIF deposition on Kaapvaal and Pilbara Cratons. *Precambrian Res.* **125**, 275–315.

Piepgras D. J. and Jacobsen S. B. (1992) The behavior of rare earth elements in seawater: Precise determination of variations in the North Pacific water column. *Geochim. Cosmochim. Acta* **56**, 1851–1862.

Planavsky N. J., Bekker A., Rouxel O. J., Kamber B., Hofmann A., Knudsen A. and Lyons T. W. (2010) Rare earth element and yttrium compositions of Archean and Paleoproterozoic Fe formations revisited: new perspectives on the significance and mechanisms of deposition. *Geochim. Cosmochim. Acta* **74**, 6387–6405.

Poulton S. W. and Canfield D. E. (2005) Development of a sequential extraction procedure for iron: implications for iron partitioning in continentally derived particulates. *Chem. Geol.* **214**, 209–221.

Quinn K. A., Byrne R. H. and Schijf J. (2006) Sorption of yttrium and rare earth elements by amorphous ferric hydroxide: influence of solution complexation with carbonate. *Geochim. Cosmochim. Acta* **70**, 4151–4165.

Rasmussen B., Krapež B., Muhling J. R. and Suvorova A. (2015) Precipitation of iron silicate nanoparticles in early Precambrian oceans marks Earth's first iron age. *Geology* **43**, 303–306.

Rasmussen B., Meier D. B., Krapež B. and Muhling J. R. (2013) Iron silicate microgranules as precursor sediments to 2.5-billion-year-old banded iron formations. *Geology* **41**, 435–438.

Rasmussen B., Muhling J. R., Suvorova A. and Krapež B. (2017) Greenalite precipitation linked to the deposition of banded iron formations downslope from a late Archean carbonate platform. *Precambrian Res.* **290**, 49–62.

Schröder S., Bedorf D., Beukes N. J. and Gutzmer J. (2011) From BIF to red beds: Sedimentology and sequence stratigraphy of the Paleoproterozoic Koegas Subgroup (South Africa). *Sedimentary Geol.* **236**, 25–44.

Sherrell R. M., Field M. P. and Ravizza G. (1999) Uptake and fractionation of rare earth elements on hydrothermal plume particles at 9 45′ N, East Pacific Rise. *Geochim. Cosmochim. Acta* **63**, 1709–1722.

Sholkovitz E. R. (1995) The aquatic chemistry of rare earth elements in rivers and estuaries. *Aquatic Geochem.* **1**, 1–34.

Smith A. J. B., Gutzmer J., Beukes N. J., Reinke C. and Bau M. (2008) Rare earth elements (REE) in banded iron formations - link between geochemistry and mineralogy. In *Ninth International Congress for Applied Mineralogy Proceedings*. Carlton, Australian Institute of Mining and Metallurgy, pp. 651–658.

Sumner D. Y. (1997) Carbonate precipitation and oxygen stratification in late Archean seawater as deduced from facies and stratigraphy of the Gamohaan and Frisco formations, Transvaal Supergroup, South Africa. *Am. J. Sci.* **297**, 455–487.

Sumner D. Y. and Bowring S. A. (1996) U-Pb geochronologic constraints on deposition of the Campbellrand Subgroup, Transvaal Supergroup, South Africa. *Precambrian Res.* **79**, 25–35.

Thurston P. C., Kamber B. S. and Whitehouse M. (2012) Archean cherts in banded iron formation: Insight into Neoarchean ocean chemistry and depositional processes. *Precambrian Res.* **214**, 227–257.

Trendall A. F. and Blockey J. (1970) The iron formations of the Precambrian Hamersley Group, Western Australia with special reference to the associated crocidolite. *Geol. Surv. Western Australia*, 366.

Trendall A. F., Compston W., Nelson D., De Laeter J. and Bennett V. (2004) SHRIMP zircon ages constraining the depositional chronology of the Hamersley Group, Western Australia. *Aust. J. Earth Sci.* **51**, 621–644.

Trendall A. F., Nelson D., Thorne A., Compston W., Williams I. and Armstrong R. (1990) Precise zircon U-Pb chronological comparison of the volcano-sedimentary sequences of the Kaapvaal and Pilbara cratons between about 3.1 and 2.4 Ga. In *Proceedings of the Third International Archaean Symposium, Perth, 1990, Extended Abstracts* (eds. J. E. Glover and S. E. Ho). Geoconferences (W.A.) Inc., Perth, pp. 81–83.

Tsikos H. and Moore J. M. (1997) Petrography and geochemistry of the Paleoproterozoic Hotazel Iron-Formation, Kalahari manganese field, South Africa; implications for Precambrian manganese metallogenesis. *Econ. Geol.* **92**, 87–97.

Tsikos H., Beukes N. J., Moore J. M. and Harris C. (2003) Deposition, diagenesis, and secondary enrichment of metals in the Paleoproterozoic Hotazel iron formation, Kalahari Manganese Field, South Africa. *Econ. Geol.* **98**, 1449–1462.

Uusitalo R. and Tuhkanen H. R. (2000) Phosphorus saturation of Finnish soils: evaluating an easy oxalate extraction method. *Agric. Food Sci. Finland* **9**, 61–70.

Van Kranendonk M. J., Webb G. E. and Kamber B. S. (2003) Geological and trace element evidence for a marine sedimentary environment of deposition and biogenicity of 3.45 Ga stromatolitic carbonates in the Pilbara Craton, and support for a reducing Archaean ocean. *Geobiology* **1**, 91–108.

Viehmann S., Bau M., Hoffmann J. E. and Münker C. (2015) Geochemistry of the Krivoy Rog Banded Iron Formation, Ukraine, and the impact of peak episodes of increased global magmatic activity on the trace element composition of Precambrian seawater. *Precambrian Res.* **270**, 165–180.

Voegelin A. R., Nägler T. F., Beukes N. J. and Lacassie J. P. (2010) Molybdenum isotopes in late Archean carbonate rocks: implications for early Earth oxygenation. *Precambrian Res.* **182**, 70–82.

von Blanckenburg F., Mamberti M., Schoenberg R., Kamber B. S. and Webb G. E. (2008) The iron isotope composition of microbial carbonate. *Chem. Geol.* **249**, 113–128.

Webb G. E. and Kamber B. S. (2000) Rare earth elements in Holocene reefal microbialites: a new shallow seawater proxy. *Geochim. Cosmochim. Acta* **64**, 1557–1565.

Zeh A., Wilson A. H. and Ovtcharova M. (2016) Source and age of upper Transvaal Supergroup, South Africa: Age-Hf isotope record of zircons in Magaliesberg quartzite and Dullstroom lava, and implications for Paleoproterozoic (2.5-2.0 Ga) continent reconstruction. *Precambrian Res.* **278**, 1–21.

Associate editor: Wolfgang Bach